

1995

Refinement and application of the URBMET mesoscale flow model to New York City

James F. Cordova
San Jose State University

Follow this and additional works at: https://scholarworks.sjsu.edu/etd_theses

Recommended Citation

Cordova, James F., "Refinement and application of the URBMET mesoscale flow model to New York City" (1995). *Master's Theses*. 1134.

DOI: <https://doi.org/10.31979/etd.x6bv-hpe2>

https://scholarworks.sjsu.edu/etd_theses/1134

This Thesis is brought to you for free and open access by the Master's Theses and Graduate Research at SJSU ScholarWorks. It has been accepted for inclusion in Master's Theses by an authorized administrator of SJSU ScholarWorks. For more information, please contact scholarworks@sjsu.edu.

INFORMATION TO USERS

This manuscript has been reproduced from the microfilm master. UMI films the text directly from the original or copy submitted. Thus, some thesis and dissertation copies are in typewriter face, while others may be from any type of computer printer.

The quality of this reproduction is dependent upon the quality of the copy submitted. Broken or indistinct print, colored or poor quality illustrations and photographs, print bleedthrough, substandard margins, and improper alignment can adversely affect reproduction.

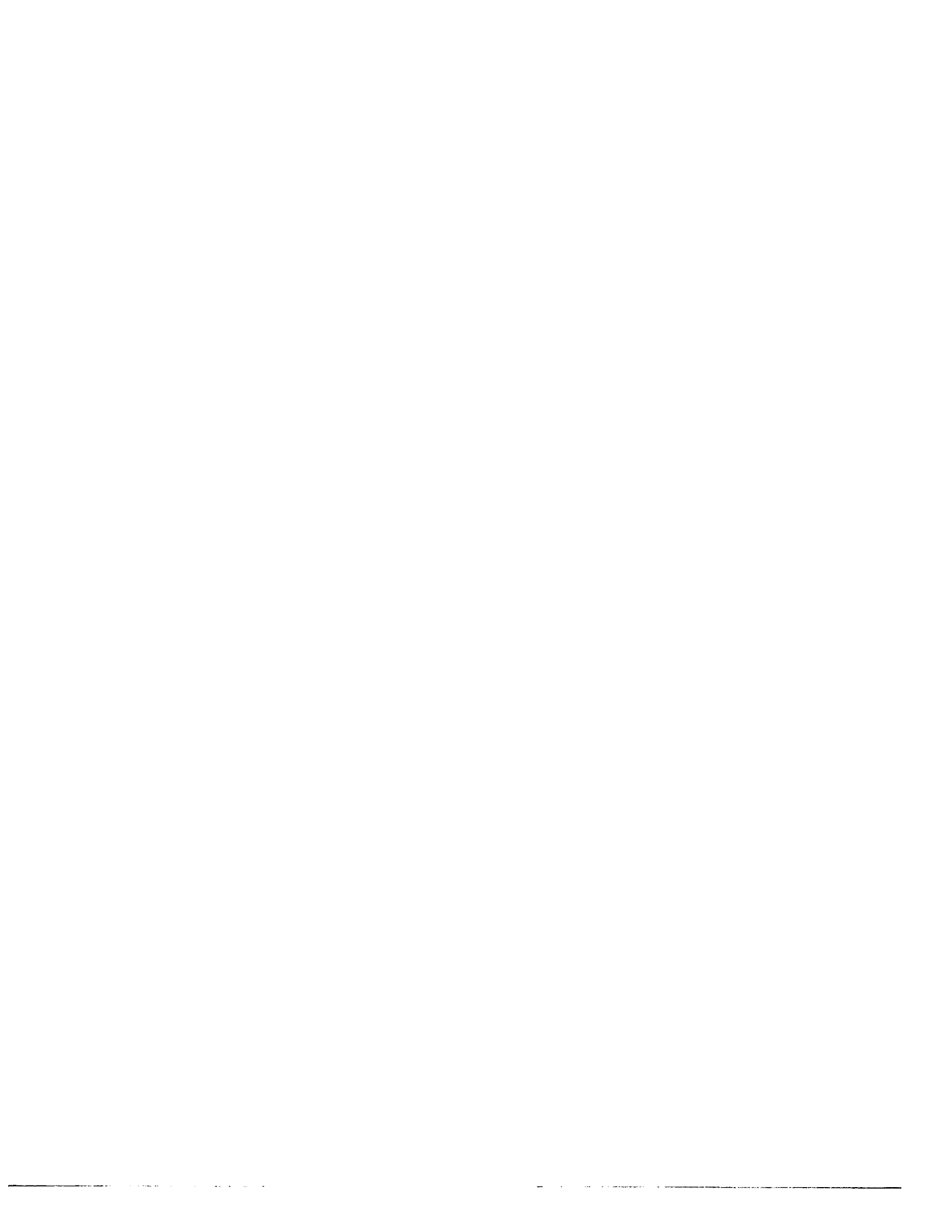
In the unlikely event that the author did not send UMI a complete manuscript and there are missing pages, these will be noted. Also, if unauthorized copyright material had to be removed, a note will indicate the deletion.

Oversize materials (e.g., maps, drawings, charts) are reproduced by sectioning the original, beginning at the upper left-hand corner and continuing from left to right in equal sections with small overlaps. Each original is also photographed in one exposure and is included in reduced form at the back of the book.

Photographs included in the original manuscript have been reproduced xerographically in this copy. Higher quality 6" x 9" black and white photographic prints are available for any photographs or illustrations appearing in this copy for an additional charge. Contact UMI directly to order.

UMI

A Bell & Howell Information Company
300 North Zeeb Road, Ann Arbor, MI 48106-1346 USA
313/761-4700 800/521-0600



**REFINEMENT AND APPLICATION OF THE URBMET MESOSCALE
FLOW MODEL TO NEW YORK CITY**

A Thesis

Presented to

The Faculty of the Department of Meteorology

San Jose State University

In Partial Fulfillment

of the Requirements for the Degree

Master of Science

By

James F. Cordova

December, 1995

UMI Number: 1377225

UMI Microform 1377225

Copyright 1996, by UMI Company. All rights reserved.

**This microform edition is protected against unauthorized
copying under Title 17, United States Code.**

UMI

**300 North Zeeb Road
Ann Arbor, MI 48103**

© 1995

James Francis Cordova

ALL RIGHTS RESERVED

APPROVED FOR THE DEPARTMENT OF METEOROLOGY

Robert Bornstein

Dr. Robert D. Bornstein

K P MacKay

Dr. Kenneth P. MacKay

Paul Halpern

Dr. Paul Halpern

APPROVED FOR THE UNIVERSITY

Serena D. Stanford

ABSTRACT

REFINEMENT AND APPLICATION OF THE URBMET MESOSCALE FLOW MODEL TO NEW YORK CITY

by James Cordova

The URBMET urban boundary layer model was improved in its lateral boundary conditions, stable surface boundary layer formulation, and initialization procedure. New lateral boundary conditions were based on the direction of the mesoscale forcing at the boundary. A new stable surface boundary layer formulation extended the range into the stable regime for which model calculations could be made. Improved initialization procedures tested new computer code for formulation, numerical, programming, and/or roundoff errors.

The model simulated the time-varying coastal planetary boundary layer in the New York City area for 9 March 1966. A parametric study consisting of two additional simulations sequentially investigated individual effects from the city and local water bodies on the New York City urban coastal environment. Model improvements enhanced the capabilities of URBMET to reproduce most of the important features of the New York City urban coastal environment during sea breeze flow conditions.

ACKNOWLEDGMENTS

I wish to express my deepest thanks to my thesis advisor, Professor Robert D. Bornstein, for his expert guidance, encouragement, time, and patience in bringing this work to completion. I would also like to thank Dr. Kenneth P. MacKay and Dr. Paul Halpern for their suggestions and support. Pursuit of my degree was made possible through the support of International Business Machines (IBM) and the Bay Area Air Quality Management District (BAAQMD). In particular, I would like to thank Mr. Robin DeMandel, my boss at the BAAQMD, for his support, encouragement and permission to use the computer facilities at work. A special thanks goes to Jeff Matsuoka of the BAAQMD for his time and expertise in helping me explain roundoff error and its relationship to how computers perform binary operations. I would also like to thank Dr. Danny Shieh for his support during my time at IBM. I am grateful to all my colleagues at San Jose State University, IBM, and the BAAQMD, who encouraged me and made available to me all their meteorological, mathematical, and computer knowledge.

My warmest thanks and love go out to my family and closest friends for their constant support. It is through them that I have learned that the true beauty of a gift is in the unconditional way it is given.

TABLE OF CONTENTS

ABSTRACT	iv
ACKNOWLEDGMENTS	v
TABLE OF CONTENTS	vi
LIST OF TABLES	vii
LIST OF FIGURES.....	viii
CHAPTER 1. INTRODUCTION.....	1
CHAPTER 2. BASIC EQUATIONS.....	6
CHAPTER 3. MODEL UPGRADES	12
a. Lateral Boundary Conditions	12
b. Stable Surface Boundary Layer.....	20
c. Initialization Procedure.....	27
CHAPTER 4. RESULTS	36
a. Run 1	36
b. Run 2	40
c. Run 3	41
CHAPTER 5. CONCLUSION	43
REFERENCES.....	47
APPENDIX A: List of Symbols.....	52
APPENDIX B: Extended Precision Registers	57

LIST OF TABLES

Table

- 1 Advantage comparison between old and new lateral boundary conditions.
- 2 Lateral boundary conditions for northwest flow.
- 3 Stable regime stability functions.
- 4 Grid point locations for centers of computational cells.
- 5 Land-type input parameters.
- 6 Model input constants.
- 7 Model input parameters.

LIST OF FIGURES

- Figure
- 1 Computational grid cell, where all symbols are defined in Appendix A.
 - 2 West to east grid configuration at western computational domain-edge ($I=1$) for closed inflow boundary condition, assuming a uniform x-direction grid spacing; see Appendix A for symbol definitions.
 - 3 Grid configuration for potential temperature for northwesterly flow conditions, where all symbols are defined in Appendix A.
 - 4 All possible inflow and outflow cases (discussed in text) at western computational domain-edge for a horizontal grid spacing of Δx .
 - 5 Stable regime stability plots.
 - 6 Interval between representable binary numbers as a function of exponent magnitude.
 - 7 Spatial distribution of potential temperature grid point locations.
 - 8 Horizontal wind velocity vectors at height 50 m at 0600 LST for Run 1.
 - 9 Values of U (cm s^{-1}) at height 50 m at 0600 LST for Run 1.
 - 10 Values of U (cm s^{-1}) at height 525 m at 0600 LST for Run 1.
 - 11 Values of w (cm s^{-1}) at height 400 m at 0600 LST for Run 1.
 - 12 Values of w (cm s^{-1}) in vertical plane through center of Manhattan at 0600 LST for Run 1.
 - 13 Horizontal wind velocity vectors at height 50 m at 1000 LST for Run 1.
 - 14 Values of U (cm s^{-1}) at height 50 m at 1000 LST for Run 1.
 - 15 Values of U (cm s^{-1}) at height 525 m at 1000 LST for Run 1.
 - 16 Values of U (cm s^{-1}) in vertical plane 21 km south of tip of Manhattan at 1000 LST for Run 1.

LIST OF FIGURES (continued)

- Figure
- 17 Values of U (cm s^{-1}) in vertical plane through center of Manhattan at 1000 LST for Run 1.
 - 18 Horizontal wind velocity vectors at height 50 m at 1400 LST for Run 1.
 - 19 Horizontal wind velocity vectors at height 1020 m at 1400 LST for Run 1.
 - 20 Values of U (cm s^{-1}) in vertical plane 21 km south of tip of Manhattan at 1400 LST for Run 1.
 - 21 Values of w (cm s^{-1}) at height 1400 m at 1400 LST for Run 1.
 - 22 Values of U (cm s^{-1}) at height 50 m at 0600 LST for Run 2.
 - 23 Values of U (cm s^{-1}) at height 525 m at 0600 LST for Run 2.
 - 24 Horizontal wind velocity vectors at height 50 m at 1000 LST for Run 2.
 - 25 Values of U (cm s^{-1}) at height 50 m at 1000 LST for Run 2.
 - 26 Horizontal wind velocity vectors at height 50 m at 1400 LST for Run 2.
 - 27 Values of w (cm s^{-1}) at height 1020 m at 1400 LST for Run 2.
 - 28 Horizontal wind velocity vectors at height 50 m at 0600 LST for Run 3.
 - 29 Values of U (cm s^{-1}) at height 50 m at 0600 LST for Run 3.
 - 30 Values of U (cm s^{-1}) at height 725 m at 0600 LST for Run 3.
 - 31 Values of w (cm s^{-1}) at height 350 m at 0600 LST for Run 3.
 - 32 Values of w (cm s^{-1}) in vertical plane through center of Manhattan at 0600 LST for Run 3.
 - 33 Horizontal wind velocity vectors at height 50 m at 1000 LST for Run 3.

LIST OF FIGURES (continued)

Figure

- 34 Values of U (cm s^{-1}) at height 50 m at 1000 LST for Run 3.
- 35 Values of U (cm s^{-1}) at height 525 m at 1000 LST for Run 3.

1. INTRODUCTION

The first three-dimensional numerical simulation of urban effects on mesoscale flow patterns concentrated on inland cities. The first of these, Vukovich et al. (1976), reproduced many observed features of the St. Louis temperature, horizontal motion, and vertical velocity fields. Model sensitivity tests by Vukovich and Dunn (1978) identified urban heat island (UHI) intensity and boundary layer stability as the controlling factors in the development of urban induced circulations, while the results of Vukovich et al. (1979) indicated that maximum ozone levels are found within UHI induced convergence zones.

Simulation of four successive days of St. Louis METROMEX data by Vukovich and King (1980) produced results that generally agreed with observed urban meteorological patterns, except during periods of changing synoptic conditions that the model formulation could not accommodate. Simulated vertical velocity distributions over St. Louis obtained by Hjelmfelt (1982) were consistent with the hypothesis that observed urban precipitation and cloud anomalies were related to perturbations arising from UHI and urban roughness effects.

Simulated St. Louis RAPS and METROMEX case studies carried out with the NCAR mesoscale model by Seaman et al. (1989) used observations to obtain space varying initial conditions, as well as time and space varying lateral boundary conditions. Results showed reduced surface evaporation associated with urbanization as the most important cause of urban-induced flow-field perturbations. The modeling study of Draxler (1986) investigated UHI influences on nocturnal wind-flow patterns in Washington, DC. Increased wind speeds and anticyclonic motion upwind of the city, as well as lee side cyclonic motions, resulted from enhanced vertical mixing as low-level air approached the warm city center and became unstable.

While the above mentioned models used gradient transport K-theory turbulence closure to study urban processes, Takano (1983) simulated Tokyo-area urban and coastal flow patterns with a second order turbulence closure model. Urban influences were included via physical parameters in the surface heat balance equation and via constant-in-time anthropogenic heating of the lowest model grid level. Results reproduced both the observed daytime UHI of 2 C° at 50 m and strong upward motion over the city. Modeled sea breeze penetration correctly stalled for several hours over the city due to an UHI-induced thermal low that produced a counter breeze on the inland city side. Modeled land breezes were, however, poorly developed, due to the flat topography formulation.

The Tokyo area wind-flow model of Kimura (1985), however, used terrain following coordinates, and provided input to a regional photochemical dispersion model. Other applications of this model included estimation of climate effects from Tokyo Bay land fill projects (Kimura and Takahashi 1990) and land-use effects on surface temperature distributions in Tokyo (Kimura and Takahashi 1991). The later application used the scheme of Kimura (1989), in which surface temperatures in grid areas with multiple land-use types are calculated from surface energy fluxes weighted by the grid fractions covered by each land-use type. Urban canopy layer processes were not addressed, since the model only calculates surface temperatures for open areas.

A non-hydrostatic urban model was applied to the Munich area using data obtained from the Stadtklima-Bayern experiment (Eichorn et al. 1988). Modeled winds and temperatures generally agreed with observed values, except in densely built up areas where differences were attributed to failure of the roughness length concept. A steady-state, neutral flow, high resolution canopy layer model was developed to overcome the above limitation. Results were presented for flows around and within a realistic building arrangement.

While the above models use a primitive equation formulation, the URBMET urban meteorology model uses a vorticity-mode formulation. The model originated as a two-dimensional, vertical plane model to simulate flow patterns over a rough, warm, dry city (Bornstein 1975). The model reproduced deceleration due to increased surface roughness at an upwind urban edge, urban heat island-induced maximum wind speed at its downwind edge, and weakened near-surface return flow downwind of the city. When a water vapor conservation equation was introduced into the model by Bornstein and Robock (1976), results demonstrated that excess anthropogenic moisture significantly increase urban buoyancy and lead to intensification of urban breezes. Reichenbacher and Bornstein (1979) studied impacts from synoptic-scale winds used as time- and space-varying upper boundary conditions for mesoscale models. Results showed that interactions between the downward and upward vertical velocities from the upper and lower boundaries, respectively, did not cause numerical instabilities.

A simplified, one-dimensional version of URBMET was modified by Dieterle (1979) to include long and short wave radiative flux divergence in the atmospheric energy equation, and a soil layer that allowed the model to simulate surface and soil temperatures from a surface energy balance. Soil evaporative flux values, as well as surface and soil moisture values, were obtained using the Halstead parameter. Santhanam (1980) replaced the Halstead parameter approach with a surface moisture balance equation to predict surface and soil moisture values.

This version of URBMET was further modified by Fruehauf (1991) to include large scale effects from a non-steady, specified upper boundary temperatures and from a steady-state subsidence velocity profile, specified to linearly decrease from a uniform value above the subsidence inversion base to zero at the surface. Results showed daytime atmospheric planetary boundary layer (PBL) height resulted from an imbalance between surface convective effects and subsidence.

URBMET was extended to three dimensions by use of second vorticity and stream function components (Bornstein et al. 1986); a higher order turbulence closure scheme was also added. The new version was used to simulate urban effects on sea breeze flows in the New York City (NYC) area (Bornstein et al. 1987a). The model was able to reproduce many observed features of rural and urban boundary layers during sea breeze and non-sea breeze periods. Wind speed maxima developed offshore due to the reduced water-surface roughness and to formation of (offshore) land breeze flows. Urban areas produced upwind regions of decreased wind speeds and downwind regions of increased wind speeds. The decreased speeds resulted from the large urban surface roughness, while the increased speeds resulted from flow acceleration over the UHI.

URBMET was transformed into the terrain-following TVM (for topographic vorticity-mode) model by Schayes and Thunis (1990) and Schayes et al. (1995) using the tensorial methods of Pielke (1984) and the sigma coordinates of Clark (1977). It has been used to simulate building barrier effects on sea breeze frontal movement over NYC (Bornstein et al. 1993) and to model interactions between sea breeze, lake breeze, and complex topographic flow regimes at Fos, France (Bornstein et al. 1995b). Recently, Thunis (1995) has developed a non-hydrostatic version of TVM to simulate mountain and gravity wave flows.

Output from URBMET simulations has also been linked to air pollution models. It was used by Bornstein et al. (1987b) as input to the Eulerian-grid numerical urban dispersion model of Shir and Shieh (1974) to simulate sulfur dioxide dispersion patterns resulting from NYC point and area sources during sea breeze flow conditions. A similar linkage by Pechinger and Seibert (1990) for Linz, Austria investigated contributions of industrial point sources to local surface sulfur dioxide concentrations.

As part of the SEVEX project, TVM provided meteorological input for a Lagrangian Monte Carlo dispersion model. Resulting concentration libraries for toxic release

scenarios under a variety of meteorological conditions were installed at all major non-nuclear point sources in Belgium as part of an operational emergency response system (Schayes and Thunis 1990; Schayes and Moyaux 1992; Delvosalle et al. 1993).

TVM has also been used to provide meteorological input to Eulerian urban photochemical models. When linked to the Urban Airshed Model (UAM)-IV by Rao et al. (1993) and Sistla et al. (1995), concentration patterns from its wind fields better located observed peak surface ozone concentrations downwind of NYC than those from observed values interpolated via the Regional Oxidant Model (ROM)-UAM interface.

In a model comparison study, wind fields from TVM, RAMS (Tripoli and Cotton 1982), and MEMO (Flassak et al. 1992), as well as those from a diagnostic mass consistent wind field model, were used as input to the California Institute of Technology (CIT) urban photochemical model of Russell et al. (1988) for the APSIS study of Athens, Greece. Results showed ozone concentrations produced from TVM wind fields were best in reproducing the time and magnitude of observed daily ozone peak values (Grossi et al. 1995).

Whereas previous applications of URBMET were successful in qualitatively reproducing mesoscale flow features, various areas of its model formulation need improvement. In addition, none of these previous studies systematically investigated nonlinear interactions between the urban and coastal processes affecting NYC flows. The current study thus involves upgrades to the URBMET formulation in the areas of lateral boundary conditions, stable surface boundary layer (SBL) formulation, and initialization procedure. In addition, it presents results from a series of simulations in which urban and ocean effects are sequentially eliminated.

2. BASIC EQUATIONS

The current study involves upgrades to the URBMET formulation in the areas of lateral boundary conditions, stable SBL formulation, and initialization procedure. In addition, it presents results from a series of simulations in which urban and oceanic effects are sequentially eliminated. Following is a summary of the formulations and assumptions used in URBMET.

Three-dimensional, time dependent calculations of velocity, temperature, and (sub-saturation) moisture in the PBL can be made with the URBMET model described by Bornstein et al. (1987a). The model consists of three layers: a constant-flux surface layer where mean field variables are one-dimensional and analytic, an upper finite differenced layer where solutions to the thermodynamic and hydrodynamic equations for atmospheric transport are numerically solved by finite differences, and a soil layer where temperature and moisture content are also numerically solved by finite differences.

The PBL equations of URBMET are derived from the exact equations of motion for a viscous, incompressible fluid in a rotating coordinate system. A set of restrictions is exacted on the equations by assuming that: the atmosphere is shallow Boussinesq (and hence incompressible) and hydrostatic, turbulence can be described by eddy coefficients (O'Brien 1970), mean thermodynamic variables are defined as sums of several parts (constant volume average, hydrostatic variability, synoptic forcing, and mesoscale forcing), sub-saturation atmospheric moisture (q) is a conserved property, radiative flux divergence (RFD) occurs only from naturally occurring gases, and potential temperature (θ) can be approximated by

$$\theta = T + \Gamma z, \quad (1)$$

where all symbols are defined in Appendix A.

After application of these assumptions, the PBL equations may be written in flux form as

$$\begin{aligned} \frac{\partial u}{\partial t} + \frac{\partial(uu)}{\partial x} + \frac{\partial(vu)}{\partial y} + \frac{\partial(wu)}{\partial z} = & -\frac{1}{\rho_a} \frac{\partial p_M}{\partial x} + f(v - v_g) \\ & + \frac{\partial}{\partial z} \left(K_m \frac{\partial u}{\partial z} \right) + K_H \left(\frac{\partial^2 u}{\partial x^2} + \frac{\partial^2 u}{\partial y^2} \right) \end{aligned} \quad (2)$$

$$\begin{aligned} \frac{\partial v}{\partial t} + \frac{\partial(uv)}{\partial x} + \frac{\partial(vv)}{\partial y} + \frac{\partial(wv)}{\partial z} = & -\frac{1}{\rho_a} \frac{\partial p_M}{\partial y} - f(u - u_g) \\ & + \frac{\partial}{\partial z} \left(K_m \frac{\partial v}{\partial z} \right) + K_H \left(\frac{\partial^2 v}{\partial x^2} + \frac{\partial^2 v}{\partial y^2} \right) \end{aligned} \quad (3)$$

$$\frac{\partial u}{\partial x} + \frac{\partial v}{\partial y} + \frac{\partial w}{\partial z} = 0 \quad (4)$$

$$0 = -\frac{1}{\rho_a} \frac{\partial p_M}{\partial z} + g \frac{(T_M + T_n)}{\theta_a} \quad (5)$$

$$\frac{\partial \theta}{\partial t} + \frac{\partial(u\theta)}{\partial x} + \frac{\partial(v\theta)}{\partial y} + \frac{\partial(w\theta)}{\partial z} = \frac{\partial}{\partial z} \left(K_h \frac{\partial \theta}{\partial z} \right) + K_H \left(\frac{\partial^2 \theta}{\partial x^2} + \frac{\partial^2 \theta}{\partial y^2} \right) + \frac{1}{\rho_a c_p} \frac{\partial Q_N}{\partial z} \quad (6)$$

$$\frac{\partial q}{\partial t} + \frac{\partial(uq)}{\partial x} + \frac{\partial(vq)}{\partial y} + \frac{\partial(wq)}{\partial z} = \frac{\partial}{\partial z} \left(K_q \frac{\partial q}{\partial z} \right) + K_H \left(\frac{\partial^2 q}{\partial x^2} + \frac{\partial^2 q}{\partial y^2} \right), \quad (7)$$

where

$$u_g = -\frac{1}{\rho_a f} \frac{\partial p_n}{\partial y} \quad (8)$$

$$v_g = \frac{1}{\rho_a f} \frac{\partial p_n}{\partial x} \quad (9)$$

define the x- and y- components of the constant geostrophic wind, respectively.

Equations (2) and (3) are recast by introduction of stream function and vorticity vectors. The principal advantage of this is elimination of pressure from the equations of motion. Use of the current stream function formulation is only possible with the incompressible flows associated with shallow Boussinesq motions (Thunis and Bornstein 1995), such as sea breeze flows and urban induced motions.

The velocity \vec{V} is related to the stream function vector $\vec{\Psi}$ by

$$\vec{V} = \nabla \times \vec{\Psi}, \quad (10)$$

in which

$$\vec{\Psi} = (\phi, -\psi, 0). \quad (11)$$

Consequently, velocity components (u, v, w) are given by

$$u = \frac{\partial \psi}{\partial z} \quad (12)$$

$$v = \frac{\partial \phi}{\partial z} \quad (13)$$

$$w = -\left(\frac{\partial \psi}{\partial x} + \frac{\partial \phi}{\partial y}\right). \quad (14)$$

Relative vorticity $\vec{\Omega}$ is defined by

$$\vec{\Omega} = \nabla \times \vec{V}, \quad (15)$$

where its components $(-\xi, \zeta, \nu)$ are thus given by

$$\xi = \frac{\partial v}{\partial z} - \frac{\partial w}{\partial y} \quad (16)$$

$$\zeta = \frac{\partial u}{\partial z} - \frac{\partial w}{\partial x} \quad (17)$$

$$v = \frac{\partial v}{\partial x} - \frac{\partial u}{\partial y}. \quad (18)$$

The hydrostatic assumption leaves only the two horizontal vorticity components (16) and (17) remaining with only their vertical terms. Thus given (10) and by employing Gaussian elimination from ξ and ζ , $\vec{\Psi}$ also simplifies to two horizontal components:

$$\xi = \frac{\partial v}{\partial z} = \frac{\partial^2 \phi}{\partial z^2} \quad (19)$$

$$\zeta = \frac{\partial u}{\partial z} = \frac{\partial^2 \psi}{\partial z^2}. \quad (20)$$

Dynamical equations for ξ and ζ can be obtained by differentiation of both (2) and (3) with respect to vertical coordinate z . Pressure can be eliminated by differentiation of (5) with respect to x and y , and by combination of the resulting equations with those for ξ and ζ , respectively. The procedure yields the following vorticity equations:

$$\begin{aligned} \frac{\partial \xi}{\partial t} = & -\frac{\partial(u\xi)}{\partial x} - \frac{\partial(v\xi)}{\partial y} - \frac{\partial(w\xi)}{\partial z} + \zeta \frac{\partial u}{\partial x} - \zeta \left(f + \frac{\partial v}{\partial x} \right) - \frac{g}{\theta_a} \frac{\partial \theta_M}{\partial y} \\ & + \frac{\partial^2}{\partial z^2} (K_m \xi) + K_H \left(\frac{\partial^2 \xi}{\partial x^2} + \frac{\partial^2 \xi}{\partial y^2} \right) \end{aligned} \quad (21)$$

$$\begin{aligned} \frac{\partial \zeta}{\partial t} = & -\frac{\partial(u\zeta)}{\partial x} - \frac{\partial(v\zeta)}{\partial y} - \frac{\partial(w\zeta)}{\partial z} + \zeta \frac{\partial v}{\partial y} + \xi \left(f - \frac{\partial u}{\partial y} \right) - \frac{g}{\theta_a} \frac{\partial \theta_M}{\partial x} \\ & + \frac{\partial^2}{\partial z^2} (K_m \zeta) + K_H \left(\frac{\partial^2 \zeta}{\partial x^2} + \frac{\partial^2 \zeta}{\partial y^2} \right). \end{aligned} \quad (22)$$

Advantages of the current hydrostatic vorticity formulations include:

- Density and pressure drop from the shallow-convection dynamic equations. The upper boundary condition on pressure is not well posed in primitive equation models, and frequently is a source of instability that generates waves extraneous to desired solutions.
- The current shallow-Boussinesq vorticity approach gives better insights into thermodynamic and dynamic processes producing mesoscale flows, as the horizontal θ -gradient terms produce vertical circulations.
- Finite differences introduce discontinuities into parameter distributions. As vortices must be integrated in space to obtain velocity fields, the order of the discontinuities is reduced by one; hence smoother velocity fields result.
- The square of vorticity (i.e., enstrophy) should be a conserved property in any mesoscale model, and thus Tripoli (1992) has reformulated the advection terms in RAMS into vorticity mode.
- All nonhydrostatic effects are automatically included in a vorticity mode model when the curl of the three-dimensional vector momentum equation is taken; some primitive equation formulations include nonhydrostatic pressure in the vertical pressure gradient term, but ignore it in the buoyancy term (Thunis and Bornstein 1995).

Limitations of the vorticity approach include:

- The vorticity approach requires an additional diagnostic integration to recover velocity components from calculated vorticity and stream function values.
- The current hydrostatic formulation only considers the vertical shear component of the two horizontal vorticity components, while it ignores the contribution of the horizontal variation of vertical velocity to these components. This assumption produces vertical velocity profiles that reach maximum values at the middle of the PBL and then remain constant with height above this level, unless a return flow region exists aloft. This effect does not significantly alter other predicted fields, except in regions of strong vertical velocity, where the hydrostatic formulation fails anyway.

URBMET employs a numerical scheme derived from the fractional step method described by Bornstein (1975) and Bornstein et al. (1986). Transport equations are solved by sequential integration of the one-dimensional advection equations, the one-dimensional diffusion equations, and finally the body-force/source terms.

Finite-difference calculations are performed on a non-uniformly spaced, three-dimensional, staggered (interlaced) Arakawa-C grid (Fig. 1), in which velocity components are located at the geometric centers of appropriate cell faces, vorticities are defined on cell edges above and below their corresponding horizontal velocities, and scalar quantities (θ and q) are located at cell geometric centers, representing volume averages.

URBMET employs donor-cell differencing for advection. While this scheme possesses many good attributes, it does introduce a significant artificial viscosity. Future versions of URBMET should investigate use of one of the newer non-damping schemes. All other terms are solved by forward-in-time, centered-in-space differencing.

3. MODEL UPGRADES

The following sections present current upgrades to the URBMET formulation in the areas of lateral boundary conditions, stable SBL formulation, and initialization procedure.

a. Lateral Boundary Conditions

Lateral boundary condition formulation in mesoscale modeling is a subject of continual investigation, because no one approach works well in all conditions. Results from previous versions of URBMET displayed numerical instabilities related to their lateral boundary condition formulations when sea breeze fronts moved to a previous inflow boundary. The current investigation thus included the reformulation of the URBMET lateral boundary conditions in a manner consistent with the flux formulation of its prognostic equations.

Horizontal boundary conditions should be both physically and mathematically consistent, and should not introduce numerical instabilities (or noise) into the model domain at either inflow or outflow boundaries. No existing formulation, however, has been able to simultaneously satisfy all three of these requirements. In a given application, these problems need to be minimized.

As lateral boundary-condition formulation is still problematic in mesoscale modeling, and as URBMET is cast in flux form, a set of flux boundary conditions for application in prognostic shallow mesoscale meteorological models is proposed. According to Thunis and Bornstein (1995), mesoscale motions are those in which the Coriolis force is large enough to determine rotational direction, but small enough to be assumed latitude independent. Such motions originate at the surface and are generally confined to the PBL.

The following concepts apply to all parameters at all non-rigid lateral and horizontal boundaries for all grid configurations and spacings. For simplicity, however, only x-direction inflow and outflow boundary conditions are discussed for θ on a uniformly spaced version of the currently used Arakawa-C grid shown in Fig. 1.

The x-direction “closed” lateral boundary condition used in previous versions of URBMET (Bornstein et al. 1987a) was

$$\frac{\partial A}{\partial x} = 0, \quad x = x_{\min} \text{ and } x_{\max}, \quad (23)$$

where A is any parameter. This condition implies constant parameter values across both inflow and outflow boundaries, i.e., mesoscale perturbations therefore can not cross such boundaries. Any term in the finite differenced version of the conservation equation for A that involves a horizontal gradient of a function containing A that produces a non-zero local change in A at either lateral boundary will thus violate of the intent of (23). Application of (23) produces two-dimensional vertical-plane solutions in each lateral boundary plane and one-dimensional vertical-profile solutions in each of the four domain corner grid columns.

As discussed above, URBMET uses a flux-formulation, three-dimensional Arakawa-C staggered grid, and a constant horizontal diffusivity. At western θ -boundary grid points (Fig. 2) for inflow conditions, Bornstein et al. (1987a) gives the following finite differenced approximations for the advection (via a Donor cell upwind algorithm) and diffusion (via centered differencing) of θ , respectively:

$$\left[\frac{\partial F_A}{\partial x} \right]_{1\frac{1}{2}} = \left[\frac{\partial}{\partial x} (u\theta) \right]_{1\frac{1}{2}} = \frac{(u_2\theta_{1\frac{1}{2}}) - (u_1\theta_{\frac{1}{2}})}{\Delta x} \neq 0 \quad (24)$$

$$\begin{aligned}
\left[\frac{\partial F_D}{\partial x} \right]_{1\frac{1}{2}} &= \left[\frac{\partial}{\partial x} \left(K \frac{\partial \theta}{\partial x} \right) \right]_{1\frac{1}{2}} = \frac{K_2 \left(\frac{\theta_{2\frac{1}{2}} - \theta_{1\frac{1}{2}}}{\Delta x} \right)_2 - K_1 \left(\frac{\theta_{1\frac{1}{2}} - \theta_{\frac{1}{2}}}{\Delta x} \right)_1}{\Delta x} \\
&= K \left[\frac{\theta_{2\frac{1}{2}} - \theta_{1\frac{1}{2}}}{(\Delta x)^2} \right] \neq 0.
\end{aligned} \tag{25}$$

The centered-differenced Boussinesq term in vorticity equation (21) is also given as:

$$\frac{g}{\theta_a} \left(\frac{\partial \theta}{\partial x} \right)_1 = \frac{g}{\theta_a} \frac{\theta_{1\frac{1}{2}} - \theta_{\frac{1}{2}}}{\Delta x} = 0. \tag{26}$$

With outflow conditions at this boundary, (25) and (26) do not change, but (24) becomes

$$\left(\frac{\partial F_A}{\partial x} \right)_{1\frac{1}{2}} = \left(\frac{\partial}{\partial x} (u\theta) \right)_{1\frac{1}{2}} = \frac{(u_1 \theta_{1\frac{1}{2}}) - (u_2 \theta_{2\frac{1}{2}})}{\Delta x}. \tag{27}$$

Consistency with condition (23) for both u and θ implies that all three of the above terms should equal zero at both inflow and outflow boundaries, but only the finite differenced Boussinesq term fulfills that criteria, i.e., all θ values west of the first known value at grid point $1\frac{1}{2}$ are assumed equal to that value. Thus $\theta_{\frac{1}{2}}$ equals $\theta_{1\frac{1}{2}}$ in (26).

The non-zero value of the finite differenced advection term, which is mathematically inconsistent with (23), arises due to the flux formulation of all advection terms in the model. The zero horizontal gradient for θ (Fig. 2) does not produce zero advection for inflow conditions, as $\partial u / \partial x$ is not zero, i.e., interior velocity u_2 does not equal boundary velocity u_1 . For outflow conditions, u_2 is again unequal to u_1 . Note that the following non-flux, first order advection formulation would be mathematically consistent with (23)

$$\left(u \frac{\partial \theta}{\partial x} \right)_{1\frac{1}{2}} = u_1 \left(\frac{\theta_{1\frac{1}{2}} - \theta_{\frac{1}{2}}}{\Delta x} \right) = 0, \tag{28}$$

as only equality between $\theta_{1\frac{1}{2}}$ and $\theta_{\frac{1}{2}}$ is required in (28).

Computed non-zero finite differenced diffusion terms in URBMET from (25) at both inflow and outflow boundaries are also mathematically inconsistent with boundary condition (23). This inconsistency occurs, as $(\partial\theta/\partial x)_2$ in (25) involves interior points not influenced by the boundary condition (Fig. 2).

Non-zero advection and diffusion values are, however, only physically inconsistent at inflow boundaries, as this implies mesoscale influences can penetrate into the model domain in violation of the assumption that external topography is horizontally homogeneous. Such non-zero values are not physically inconsistent at outflow boundaries, however, as mesoscale influences can leave the domain and move over the assumed horizontally homogeneous external topography.

Use of large fetchs downwind of internal surface discontinuities would allow resulting mesoscale perturbations to dampen before they encounter a downwind boundary. In complex terrain simulations, however, it is frequently impossible to place lateral boundaries far from significant topographic features, and hence imposed boundary conditions must allow mesoscale perturbations to leave the domain without creation of numerical problems.

In summary, the mathematical intent of old URBMET lateral boundary condition (23) to prevent mesoscale perturbations from crossing any lateral boundary was first subverted at both inflow and outflow boundaries by use of flux formulation advection terms. This intent will also always be subverted at both inflow and outflow boundaries with use of finite differenced horizontal diffusion terms. It was thus necessary in the original version of URBMET to arbitrarily assign zero values to advection and diffusion terms at any inflow or outflow lateral boundary, and thus not to evaluate their finite differenced ver-

sions. This introduced inconsistency, as computed finite differenced values would not have been zero.

Finally, the original intent of (23), to prevent mesoscale perturbations from crossing any lateral boundary, is reasonable only for inflow boundaries. For outflow boundaries, mesoscale perturbations should numerically exit the computational domain, which physically exist, even over an assumed homogeneous terrain downwind of the domain.

The new lateral boundary conditions in URBMET are thus specified, not on basic prognostic parameters, but on their advective and diffusive fluxes. In addition, different conditions are applied at inflow and outflow boundaries, i.e. at the former,

$$\frac{\partial}{\partial x}(F_A) = \frac{\partial}{\partial x}(F_D) = 0, \quad \text{at } x = x_{IN}. \quad (29)$$

These conditions still produce closed inflow conditions, consistent with the assumed horizontally homogeneous upwind terrain. The finite difference approximations for both the x-direction advection and diffusion of θ [(24) and (25), respectively] are thus again arbitrarily set to zero, as with the old boundary conditions. A zero value for the finite differenced Boussinesq term still results at inflow boundaries, even though upwind differencing is now used for this term, e.g. at the western boundary (Fig. 2)

$$\frac{g}{\theta_a} \left(\frac{\partial \theta}{\partial x} \right)_1 = \frac{g}{\theta_a} \frac{\theta_1 - \theta_0}{\Delta x} = 0. \quad (30)$$

Since only diffusion is a second order operation, a second computational boundary condition is allowed only on this term; hence, open conditions exist for the advection and Boussinesq terms. Numerical evaluation of these terms produce non-zero mesoscale perturbations that exit outflow boundaries. The following new closed outflow boundary condition is thus only applied to F_D :

$$\frac{\partial}{\partial x}(F_D) = 0, \quad \text{at } x = x_{\text{OUT}}. \quad (31)$$

The grid configuration for θ under northwesterly flow conditions is shown in Fig. 3. Note that, while (29) and (31) produce two-dimensional vertical plane solutions in inflow planes, solutions in outflow planes are thus quasi three-dimensional due to the non-zero advection and/or Boussinesq terms directed perpendicular to the boundary. Inflow corner vertical grid-columns are still one-dimensional, but outflow corner columns are also quasi three-dimensional. Note that "transitional" corner grid columns at the intersections between horizontal inflow and outflow boundary planes only have non-zero horizontal derivatives perpendicular to their outflow plane.

As the outflow finite difference version of (31) at the western boundary is still the same as with (25), diffusion must again be arbitrarily set to zero at outflow boundaries. The finite difference approximation for the Boussinesq term at the western boundary for outflow conditions is

$$\frac{g}{\theta_a} \left(\frac{\partial \theta}{\partial x} \right)_1 = \frac{g}{\theta_a} \frac{\theta_1 - \theta_2}{\Delta x} \neq 0. \quad (32)$$

This term is now non-zero with upwind differencing, as it involves unequal θ_1 and θ_2 values. The corresponding Donor cell finite difference equation is still given by (27), but the new formulation keeps resulting non-zero advective flux-divergence values.

Comparison of the advantages and disadvantages of the new and old horizontal boundary conditions (Table 1) shows that for inflow cases, the two sets of conditions are identical. The advection and diffusion terms must be forced to zero in both cases for consistency with the assumption of horizontally homogeneous upwind external terrain, but the Boussinesq term is zero in both cases without any assumptions.

Comparison of outflow conditions shows zero diffusion values imposed in both the old and new cases. The old boundary condition, however, overspecified the first-order advection and Boussinesq terms, for which conditions can only be applied at inflow boundaries. The new outflow condition, however, is applied neither to the advection term (consistent with its mathematical order) nor to the Boussinesq term (as the new condition is applied only to fluxes). The new upwind differencing scheme for the Boussinesq term thus correctly produces zero values only at inflow boundaries. Overall, therefore, the new horizontal boundary conditions are an improvement over the old formulation, as they are second order for diffusion and first order for advection, which allows mesoscale perturbations to advect out of the domain under outflow conditions.

The current formulation also clarifies the proper boundary conditions when synoptic and mesoscale forcings at lateral boundaries are either complementary or in opposition. All six possible perpendicularly directed mesoscale and synoptic boundary flow combinations are shown in Fig. 4, in which the direction and magnitude of the mesoscale forcing at θ -grid point $1\frac{1}{2}$ can be determined by subtraction of the vector wind at grid point 1 from that at grid point 2. The Strong Outflow and Weak Inflow cases have outward directed mesoscale forcings; the Weak Outflow, Strong Inflow, and Divergent Flow cases have inward directed forcings; while the Convergent Flow case has no mesoscale forcing.

Based on the obvious criterion of an outflow wind direction at grid point 1, open outflow boundary conditions (in which mesoscale perturbations would be allowed to exit the domain via computed non-zero values of the above discussed finite differenced terms) should be applied for three of the cases (Fig. 4). The current formulation, however, proposes that closed inflow (i.e., zero valued mesoscale perturbation) boundary conditions should be applied only at one of these three, i.e., Weak Outflow case. As its mesoscale forcing is inward directed, it would therefore be incorrect to compute a non-zero inward directed mesoscale perturbation. Such a perturbation would reflect back into the domain

against the outflow lateral boundary velocity, and would thus create extraneous destructive numerical wave-like perturbations. This criterion cannot be applied to the (outflow) Divergent Flow case because its mesoscale influences must (for mass consistency) move inward as well as outward.

Likewise, again based on the obvious criterion of an inflow wind direction at grid point 1, closed inflow boundary conditions (in which mesoscale perturbations would not be allowed to enter the domain via assumed zero values of the above discussed finite differenced terms) should be applied for the other three cases. The current formulation proposes, however, that closed inflow boundary conditions should be applied only at one of these three, i.e., the Strong Inflow case. Of these three cases, only its mesoscale forcing is inward directed, and thus must be suppressed to prevent violation of the assumed upwind horizontally homogeneous terrain. This suppression cannot be applied to the Convergent Flow case because its mesoscale influence results from interior as well as exterior boundary influences. This suppression also can not be applied to the Weak Inflow case, as its mesoscale forcing is outward directed. If prevented from leaving, a build up of energy would result at the boundary.

In summary, as Fig. 4 shows, clarification of the concept of "strong" versus "weak" inflow and outflow cases produces new lateral boundary conditions based only on the direction of its mesoscale forcing, not on the direction of the resultant (large scale plus mesoscale) boundary flow. Only for the "strong" inflow and outflow cases (mesoscale and large scale boundary flows in same direction) are the inflow and outflow boundary conditions applied, respectively. For the corresponding "weak" inflow and outflow cases (mesoscale and large scale boundary flows in opposite directions), outflow and inflow boundary conditions are applied, respectively.

New boundary conditions (29) and (31) also impact vertical velocity w values, given by,

$$w = - \int_0^z \left(\frac{\partial u}{\partial x} + \frac{\partial v}{\partial y} \right) dz . \quad (33)$$

Effects of the new conditions on the calculation of w for all inflow, outflow, and corner grid points for the northwesterly flow case of Fig. 3 are shown in Table 2. As described above, the new conditions produce two-dimensional vertical plane solutions at all inflow horizontal boundaries and only quasi (because of the zero-valued horizontal diffusion term) three-dimensional solutions at outflow horizontal boundaries.

All horizontal gradients are zero at the inflow corner point, producing a zero w -value. For the East to West and North to South inflow boundaries, y - and x -derivatives are zero, respectively, and thus w is calculated from only $\partial u/\partial x$ and $\partial v/\partial y$, respectively. For the East to West and North to South outflow boundaries, neither gradient is zero, and hence w is calculated using both terms in (33); this is also true for the outflow corner grid point. Inflow conditions take precedence at both transition corner grid points, i.e., w is calculated from $\partial u/\partial x$ at the NE point and from $\partial v/\partial y$ at the SW point.

In summary, even though the new lateral boundary conditions are posed on flux quantities, imposed simplifications in solution dimensionality result in the elimination (for consistency) of terms in the correct calculation of w values at various lateral boundary grid points.

b. Stable Surface Boundary Layer

Monin-Obukhov similarity theory is used in mesoscale models to scale both non-neutral surface boundary layer (SBL) turbulent fluxes and mean wind speed, temperature,

and specific humidity gradients. Atmospheric stability is determined from the Monin-Obukhov length L , given by

$$L = \frac{u_*^2 \theta_a}{g k_o \theta_*}. \quad (34)$$

In an unstable SBL, L is the level at which buoyancy production of turbulent kinetic energy (TKE) first becomes greater than shear production, while in a stable SBL it is the level at which shear effects on turbulence are overwhelmed by buoyancy destruction.

SBL vertical gradients of U , θ , and q are given, respectively, by

$$\frac{\partial U}{\partial z} = \frac{u_*}{\ell} \phi_m^* \quad (35)$$

$$\frac{\partial \theta}{\partial z} = \frac{\theta_*}{\ell} \phi_h^* \quad (36)$$

$$\frac{\partial q}{\partial z} = \frac{q_*}{\ell} \phi_h^*, \quad (37)$$

where ϕ_m^* and ϕ_h^* are nondimensional atmospheric stability functions of z/L . Note that the two thermodynamic functions are assumed equal. Prandtl turbulent mixing length ℓ is given by

$$\ell = k_o z, \quad (38)$$

where the von Karman constant k_o is generally taken as 0.4. As the above gradients become unbounded at the surface, numerical models frequently use the following alternative expression for ℓ :

$$\ell = k_o (z + z_0). \quad (39)$$

The resulting dimensionless ratio

$$\frac{z + z_0}{L} \quad (40)$$

thus produces bounded surface gradients.

Monin-Obukhov (1954) proposed that both non-dimensional stability functions be given as

$$\phi^* = \phi_m^* = \phi_h^* = 1 + \beta \left(\frac{z}{L} \right), \quad -0.03 < \frac{z}{L} \ll 1 \quad (41)$$

for a "close to neutral" SBL.

Analysis by Businger et al. (1971) of the Kansas data set lead to derivation of unequal expressions for ϕ_m^* and ϕ_h^* and to a k_0 of 0.35. In addition, the ratio of the eddy heat and momentum diffusivities under neutral conditions was calculated as approximately 1.35, as compared to its generally accepted value of 1.0. The new value arose as their neutral ϕ_h^* did not equal 1.0, but was 0.74.

Unstable condition stability functions were given as

$$\phi_m^* = \left[1 - 15 \left(\frac{z}{L} \right) \right]^{-\frac{1}{4}}, \quad \frac{z}{L} < 0 \quad (42)$$

$$\phi_h^* = 0.74 \left[1 + 9 \left(\frac{z}{L} \right) \right]^{-\frac{1}{2}}, \quad \frac{z}{L} < 0, \quad (43)$$

while stable condition expressions were

$$\phi_m^* = 1 + 4.7 \left(\frac{z}{L} \right), \quad \frac{z}{L} > 0 \quad (44)$$

$$\phi_h^* = 0.74 + 4.7 \left(\frac{z}{L} \right), \quad \frac{z}{L} > 0. \quad (45)$$

URBMET originally employed the above Businger et al. stability functions; however, for stable conditions, simulated turbulence values decreased too quickly because the functions grew rapidly beyond $z/L = 0.5$.

To demonstrate why turbulence is suppressed in stable regimes, (41) can be rewritten in terms of Richardson number Ri:

$$Ri = \frac{g}{\theta_a} \frac{\partial \theta / \partial z}{(\partial U / \partial z)^2}. \quad (46)$$

Under stable conditions,

$$\frac{z}{L} = \frac{Ri}{1 - \beta Ri}, \quad (47)$$

and thus (41) becomes

$$\phi^* = (1 - \beta Ri)^{-1}. \quad (48)$$

Buoyancy destruction of turbulence in stable conditions overcomes shear production at the critical Ri, which from (48) is given as

$$Ri_c = \beta^{-1} = 0.2. \quad (49)$$

In terms of z/L , (47) and (49) show the corresponding critical z/L value as

$$\left(\frac{z}{L} \right)_c = \infty. \quad (50)$$

Shir and Bornstein (1977) discussed techniques to extend the region of applicability of (44) and (45) to greater z/L values. They noted the variety of methods used by PBL modelers to prevent turbulence from dying so quickly (i.e., at $Ri = 0.2$). The finite-differenced version of (46)

$$Ri_{\Delta} = \frac{g}{\theta} \frac{\Delta x}{(\Delta u)^2} (\Delta z) \quad (51)$$

shows Ri_c (and hence β) as both functions of layer depth Δz . The most common method thus employed by modelers (whose vertical grid spacings can range up to 100 m) is to use values of β smaller than those derived from short (16 m) tower observations, i.e., McPherson (1970) used a value of 0.03, Neumann and Mahrer (1971) used 0.3, and Estoque (1961) used 1.0.

A first attempt to develop stability functions valid for more stable conditions was that by Webb (1970), who analyzed the data from O'Neill and Australia (at Kerang and Hay). He proposed equal stability functions given as

$$\phi^* = 1 + 5.2 \left(\frac{z}{L} \right), \quad \frac{z}{L} < 1 \quad (52)$$

$$= 1 + \beta, \quad 1 \leq \frac{z}{L} \leq 6. \quad (53)$$

Note the proposed extension beyond $(z/L) = 1$ produces a new log-law regime.

Clarke (1970a) extended the Webb results to more stable conditions (using the same Australian measurements) via an integral function. Carson and Richards (1978) recast this function in terms of the following ϕ^* :

$$\phi^* = \frac{1 + 5\left(\frac{z}{L}\right)}{1 + 0.0079\left(\frac{z}{L}\right)\left[1 + 5\left(\frac{z}{L}\right)\right]}, \quad \frac{z}{L} < 1 \quad (54)$$

$$= \frac{1 + 5}{1 + 0.0079\left(\frac{z}{L}\right)[1 + 5]}, \quad 1 \leq \frac{z}{L}. \quad (55)$$

The low k_0 value proposed by Businger et al. probably arose from instrument inadequacies (Högström 1988). Based on observations from Sweden, he concluded that $k_0 = 0.4 \pm 0.01$, and that the neutral-stability heat to momentum eddy diffusivity ratio was 0.95 ± 0.04 . From these results, he then derived the following new stable regime equations for ϕ_m^* and ϕ_h^* ,

$$\phi_m^* = 1 + 6\left(\frac{z}{L}\right), \quad \frac{z}{L} \leq 0.5 \quad (56)$$

$$\phi_h^* = 1 + 7.8\left(\frac{z}{L}\right), \quad \frac{z}{L} \leq 0.5. \quad (57)$$

No relationship was given for $z/L > 0.5$ (because of a scarcity of data), but he did note that values started to level out within the range of $0.5 < z/L < 1$, consistent with (52).

The equations of Hicks (1976), also modified by Carson and Richards (1978), did extend the Businger functions out to more stable values. Hicks had indicated that it was possible that $\phi_m^* = 2\phi_h^*$ in extreme stable conditions, but this relationship could not be confirmed. Carson and Richards thus assumed that ϕ_m^* and ϕ_h^* were equal and given by:

$$\phi^* = 1 + 5\left(\frac{z}{L}\right), \quad 0 \leq \frac{z}{L} \leq 0.5 \quad (58)$$

$$= 8 - 4.25\left(\frac{z}{L}\right)^{-1} + \left(\frac{z}{L}\right)^{-2}, \quad 0.5 < \frac{z}{L} \leq 10 \quad (59)$$

$$\phi^* = 0.76 \left(\frac{z}{L} \right), \quad 10 < \frac{z}{L}. \quad (60)$$

Using data from Cabauw (The Netherlands), Holtslag and DeBruin (1988) fit a single function to (58) to (60), which (in the form of the integrated correction to the log law ψ_m^*) is

$$\psi_m^* = - \left[\beta_1 \left(\frac{z}{L} \right) + \beta_2 \left(\frac{z}{L} - \frac{\beta_3}{\beta_4} \right) \exp \left(-\beta_4 \frac{z}{L} \right) + \frac{\beta_2 \beta_3}{\beta_4} \right]. \quad (61)$$

When differentiated by Martien (1991), (61) gives

$$\phi_m^* = \phi_h^* = 1 + \beta_1 \frac{z}{L} + \beta_2 \frac{z}{L} \left(1 + \beta_3 - \beta_4 \frac{z}{L} \right) e^{-\beta_4 \frac{z}{L}}. \quad (62)$$

Holtslag and DeBruin stated that because of intermittent turbulence in the nocturnal boundary layer, (62) produces less reliable results for $z/L \geq 7$.

Stability function extensions discussed above are summarized in Table 3 and plotted in Fig. 5. Note that the Businger et al. (1971) function rises rapidly, while the others start to level out at $z/L = 1$. While the Webb (1970) and Högström (1988) functions become constant at $z/L = 1$, the Clarke (1970a) function actually decreases for $z/L > 1$. The transition points of the Carson and Richards (1978) functions are clearly visible at $z/L = 0.5$ and 10 . The single function of Holtslag and DeBruin (1988) is very similar to Carson and Richards, but without any sharp transition points. The stability functions in (58) through (60) were adopted in the current simulations, as (62) was unknown to the author at the time. It will be incorporated into URBMET in the future because of its ability to handle a wide range of stabilities with a single smooth function.

c. Initialization Procedure

Initialization of URBMET involves two phases. The first is an error analysis procedure in which new computer code is tested for formulation, numerical, or programming errors. The test consists of the executing the full three-dimensional model equations over an assumed homogeneous terrain, and verifying that all vertical velocity values across the domain still compute as zero. The second phase consists of computing a neutral stability, steady-state solution of the full three-dimensional model equations over a prescribed distribution of surface roughness $z_0(x,y)$. After completing this phase, the actual non-neutral simulation begins with a "spin-up" period.

Errors can be introduced during code development from any of the following: coding, specified boundary conditions, and use of a staggered grid, non-uniform grid spacings, and time splitting. Eliminating these errors during Phase 1 of the URBMET initialization procedure may not ensure a non-zero vertical velocity field over an assumed horizontally homogeneous topography due to effects from computer roundoff.

Use of w as the Phase 1 benchmark-parameter is logical, as it is calculated at the culmination of the model solution procedure. Vertical velocity values should be uniformly zero over homogeneous terrain, as shown by (33). Non-zero w -values will result from any error that produces non-zero gradients in u or v over homogeneous terrain. This further corrupts the horizontal wind field via the third term on the right-hand sides of (21) and (22).

Computer roundoff errors in URBMET arose from its numerical averaging and differentiation algorithms, which are floating point operations for non-integer numerical procedures. Any real number according to Goldberg (1991) can be represented in floating point form, with base B (always assumed even) and precision P (number of significant digits). The general form of a floating point number is thus

$$\pm(d_0 B + d_1 B^{-1} + \dots + d_{P-1} B^{-(P-1)}) B^e, \quad 0 \leq d_i < B, \quad (63)$$

where e is the exponent, whose boundaries are discussed below. Floating point numbers are often normalized ($0 < d_0 < B$) to ensure standardization of representation. For example, for $B = 10$ and $P = 4$, the number 0.1043 is represented as

$$\left[(1 \times 10^0) + (0 \times 10^{-1}) + (4 \times 10^{-2}) + (3 \times 10^{-3}) \right] 10^{-1}, \quad (64)$$

whose normalized form is 1.043×10^{-1} . Without normalization, 0.01043×10^1 also represents 0.1043.

Goldberg states that most real numbers cannot be exactly represented by the fixed number of binary digits computers use to store a real number. This occurs, for example, when the absolute value of a real number is beyond the range that can be represented by the computer, i.e., either larger than $B \times B^{e_{max}}$ or smaller than $1.0 \times B^{e_{min}}$, where e_{max} and e_{min} are the largest and smallest representable exponents, respectively. Note that e_{max} and e_{min} are dependent on "bit number," as discussed below. These occurrences are referred to as overflow and underflow, respectively.

This also occurs when the real number lies between two consecutive representable numbers (Burden and Faires 1985). Consider for example, the computer representation of a floating-point number by a hypothetical binary ($B = 2$) machine that consists of a: 1-digit (bit) sign indicator (0 for positive and 1 for negative numbers), 4-bit exponent, and 9-bit mantissa (fractional part of number). Such a small mantissa, of course implies a coarse interval between representable numbers. The 4-bit exponent has a range of 0 to 16, but actually must be -8 to +7 (including zero) to allow for numbers smaller than ± 1.0 ; thus the computer subtracts 8 from all exponents.

Binary machine numbers can also be normalized by setting the first mantissa bit to one. Consider for example, the following number represented within the above hypothetical computer:

$$\boxed{0 \mid 1110 \mid 100000010}, \quad (65)$$

where the number is positive (indicated by leftmost 0 bit) and normalized (indicated by leading 1 in mantissa). The exponent (1110) is equivalent to decimal number

$$(1 \times 2^3) + (1 \times 2^2) + (1 \times 2^1) + (0 \times 2^0) = 14, \quad (66)$$

while the mantissa (final 9 bits) is

$$\begin{aligned} & [1 \times (1/2)^0] + [0 \times (1/2)^1] + [0 \times (1/2)^2] + [0 \times (1/2)^3] + [0 \times (1/2)^4] + \\ & [0 \times (1/2)^5] + [0 \times (1/2)^6] + [1 \times (1/2)^7] + [0 \times (1/2)^8]. \end{aligned} \quad (67)$$

Given the values in Appendix B, this is equivalent to decimal number

$$\left[(1/2)^0 + (1/2)^7 \right] 2^{14-8} = 64.5. \quad (68)$$

The next smallest binary number

$$\boxed{0 \mid 1110 \mid 100000001} \quad (69)$$

corresponds to decimal number

$$\left[(1/2)^0 + (1/2)^8 \right] 2^{14-8} = 64.25, \quad (70)$$

while and the next highest binary number

$$\boxed{0 \mid 1110 \mid 100000011} \quad (71)$$

corresponds to decimal number

$$\left[(1/2)^0 + (1/2)^7 + (1/2)^8 \right] 2^{14-8} = 64.75 . \quad (72)$$

Binary numbers in this example thus have an interval between representable numbers of 0.25. For a given mantissa size, however, this interval decreases as exponent magnitude decreases (Fig. 6).

To ensure that any non-zero representable number is approximated by the closest representable number, computers have special registers with extended mantissas to allow for temporary storage of more precise numbers. Any number subsequently transferred into a permanent register is thus an approximation of the temporary extended-precision number. The approximation is obtained by a rounding process that involves a chopping step, in which the extra bits in temporary registers are eliminated. For example, if a computer has three extra bits in its temporary register, then the non-representable number 64.95 would be approximated by

$$\boxed{0 \mid 1110 \mid 100000011111} , \quad (73)$$

which in decimal form (Appendix B) is

$$\left[(1/2)^0 + (1/2)^7 + (1/2)^8 + (1/2)^9 + (1/2)^{10} + (1/2)^{11} \right] 2^{14-8} = 64.96875 . \quad (74)$$

Rounding evaluates the temporary bits to determine if the resulting binary extension is greater than, equal to, or less than the mid-point of the interval between the adjacent two representable numbers. If greater, the computer increments the extended mantissa by 1, and chops the temporary bits. When less, only chopping occurs. Note, com-

puter engineers decide which procedure to carry out when a temporary binary number equals a mid-point value.

In the current example, the mid-point value is

$$\boxed{0 \mid 1110 \mid 00000000100} , \quad (75)$$

which corresponds to the decimal number 0.125. In binary representation, the input number 64.95, initially approximated by (73), has three final mantissa bits with a value greater than the mid-point value of binary number 100. Adding 1 to the mantissa produces

$$\boxed{0 \mid 1110 \mid 10000100000} . \quad (76)$$

Chopping drops the temporary three bits, and results in binary number

$$\boxed{0 \mid 1110 \mid 100000100} . \quad (77)$$

Its decimal equivalent,

$$\left[(1/2)^0 + (1/2)^6 \right] 2^{14-8} = 65.0 , \quad (78)$$

is only 0.05 more than the original input value. The resulting error is called round-off.

Since most real numbers cannot be exactly represented by the finite number of computer binary digits, inputs and/or calculations usually involve inexact representations of intended values, e.g., consider the addition of nonrepresentable 64.47 and representable 0.25 on the current hypothetical computer. For simplicity, decimal equivalents of the binary numbers will be used. Since 64.47 is not exactly representable, it will be approximated (via rounding) by the nearest number: 64.50. The sum of 0.25 and 64.50 thus produces an error of 0.03.

A coding application of the knowledge that only some real numbers are representable on any given computer is to make floating-point logical tests with mathematical intervals rather than absolute values. Computers have built-in safeguards to minimize round-off errors. Programmers are thus faced with devising methods to deal with remaining errors, which unchecked can grow and propagate to destroy a numerical solution.

Problems also result when a uniform parameter field does not yield either zero gradients or average values equal in magnitude to the constant value. Such computer roundoff errors in averaging and differentiation schemes in URBMET were identified and eliminated as follows.

An x-direction averaged u-value at point i, for example, is given by

$$u_p(i) = \frac{\Delta x_E(i) u(i+1) + \Delta x_W(i) u(i)}{\Delta x_E(i) + \Delta x_W(i)}, \quad (79)$$

where

$$\Delta x_E(i) = x(i+1) - x(i) \quad (80)$$

$$\Delta x_W(i) = x(i) - x(i-1). \quad (81)$$

In a uniform grid:

$$\Delta x_E = \Delta x_W = \Delta x, \quad (82)$$

$$u_p(i) = \frac{u(i+1) + u(i)}{2}. \quad (83)$$

When no gradient of u exists,

$$u(i+1) = u(i) = \bar{u}(i), \quad (84)$$

which results in

$$u_p(i) = \bar{u}(i). \quad (85)$$

With the non-uniform grid of URBMET, computer roundoff could lead to

$$u_p(i) = \left[\frac{\Delta x_E}{\Delta x_E + \Delta x_W} + \frac{\Delta x_W}{\Delta x_E + \Delta x_W} \right] \bar{u}(i) \neq 0, \quad (86)$$

when the sum of the two weights in (86) do not sum exactly to unity. This would result due to computer roundoff error describe above, when $(\Delta x_E)_i$ and/or $(\Delta x_W)_i$ are not representable numbers. The solution to this problem is to set

$$u_p(i) = \bar{u}(i), \quad \text{if } u(i+1) = u(i) \quad (87)$$

at all such averages within the code.

The second problem area involved derivatives on the non-uniform URBMET grid, e.g., the x derivative for θ is given by

$$\left(\frac{\partial \theta}{\partial x} \right)_i = W_1(i) \cdot \theta(i+1) + W_2(i) \cdot \theta(i) - W_3(i) \cdot \theta(i-1), \quad (88)$$

where

$$W_1(i) = \frac{\Delta x_W(i)}{\Delta x_E(i) [\Delta x_W(i) + \Delta x_E(i)]} \quad (89)$$

$$W_2(i) = \frac{\Delta x_E(i) - \Delta x_W(i)}{\Delta x_E(i) + \Delta x_W(i)} \quad (90)$$

$$W_3(i) = \frac{\Delta x_E(i)}{\Delta x_W(i) [\Delta x_W(i) + \Delta x_E(i)]}. \quad (91)$$

In a uniform grid, described by (82):

$$W_1(i) = W_3(i) = \frac{1}{2\Delta x},$$

$$W_2(i) = 0.$$
(92)

When no gradient of θ exists,

$$\frac{\partial \theta}{\partial x} = \frac{\theta(i+1) - \theta(i-1)}{2\Delta x} = 0,$$
(93)

if

$$\theta(i+1) = \theta(i-1) = \theta.$$
(94)

With the non-uniform grid of URBMET, computer roundoff could lead to a non-zero derivative in (93) if

$$W_1(i) \neq W_3(i)$$

$$W_2(i) \neq 0$$
(95)

and

$$\frac{\partial \theta}{\partial x} = [W_1(i) + W_2(i) - W_3(i)]\theta \neq 0,$$
(96)

when $W_1(i)$, $W_2(i)$, and/or $W_3(i)$ were again non-representable numbers. The solution to this problem is to set

$$\frac{\partial \theta}{\partial x} = 0, \quad \text{if } \theta(i+1) = \theta(i-1) = \theta(i)$$
(97)

at all such derivatives within the code.

The first step of Phase 2 of the URBMET initialization procedure involves construction of a vertical analytical PBL Ekman wind spiral profile from constant specified values of \bar{U}_g , eddy viscosity K , and PBL height. Above-PBL winds are set equal to \bar{U}_g .

The next step involves calculating an equilibrium, one-dimensional, numerical solution of the horizontal-momentum equations over each surface grid point, starting with a prescribed distribution of $z_0(x,y)$ and the above mentioned Ekman spirals. Equilibrium is reached when the maximum horizontal acceleration over the domain becomes smaller than a prescribed value.

The three-dimensional phase of the initialization procedure involves calculating equilibrium solutions for vorticity (21) and (22) over inhomogeneous terrain (including advective effects), starting with the above mentioned one-dimensional equilibrium solutions. Three-dimensional equilibrium is reached when the maximum vertical acceleration over the domain is smaller than a prescribed value.

The last step of this phase is to “spin up” the model using the complete set of three-dimensional, non-neutral, equations for about six hours preceding the start of the period of interest to allow for damping of noise resulting from initiating the non-neutral solution.

In summary, this section discussed numerous upgrades to the URBMET model associated with three areas of its formulation: lateral boundary conditions, stable SBL formulation, and initialization procedure. The following section shows results from the application of the new version of the model, but does not attempt to relate improvements in its results too any specific upgrade.

4. RESULTS

The date 9 March 1966 was selected for simulation because sea breeze frontal development was documented by a significant amount of observational meteorological data. The simulation was begun at 1800 LST on the previous day to allow for model “spin up.” Model input parameters are summarized as follows: grid point locations (Fig. 7 and Table 4), land-type parameters (Table 5), constants (Table 6), and parameters (Table 7).

Flow conditions in the NYC area throughout 9 March were dominated by an anti-cyclone located NW of the area. This produced northwesterly geostrophic winds throughout the day. Note that, while this flow was used as the constant upper boundary condition, the model produced wind fields at the lateral boundaries consistent with (29) and (31).

The three simulations carried out consisted of an initial run that included all urban and ocean areas, a run in which all urban areas were eliminated, and a run in which the Atlantic Ocean and Long Island Sound (LIS) were eliminated. Thus, impacts associated with each of the main forcings are sequentially investigated. Results were compared to the observational analysis in Bornstein (1987), the two-dimensional URBMET simulations of Bornstein (1975), and the three-dimensional URBMET simulations of Bornstein et al. (1987a), whose domain was smaller than currently used.

a. Run 1

Simulated 0600 LST winds were offshore due to a combination of the geostrophic and land breeze flows (Fig. 8). Horizontal flow vectors at the lowest finite differenced grid point (50 m) also show an offshore acceleration due to reduced surface roughness over the water. A slight turning of the flow and an offshore confluence are also seen

downwind of the city in the southeast domain corner. This confluence, due to urban effects (as will be seen in Run 3 results), was not seen in the results of Bornstein et al. (1987a) because the current domain is extended to the south and east.

Total horizontal wind speed values U at 50 m (Fig. 9) double in magnitude in both offshore regions (Ocean and LIS), with strong gradients along shorelines. Urban influences are evidenced by the curves in the 2 m/s isopleth over the urban center, in which an UHI induced maximum speed area is located NE of a roughness induced minimum speed area. The near-shore bow of slower values SE of the urban center is due to advection of its roughness effect, while the larger downwind offshore bow of low speeds is due to the urban induced confluence of Fig. 8. These urban influences (without the complicating effects of local water bodies) were found in the two-dimensional simulations of Bornstein (1975), in which the roughness effect led to reduced speeds over upwind urban grid points and in which the UHI effect produced high values over downwind urban areas. These results are consistent with observed speed changes found by Bornstein (1987) along streamlines passing through the center of NYC.

The horizontal extent of each urban influence region is unclear in these Run 1 results, because they interact with water-body induced accelerations in regions NE and S of the city. In the small-domain results of Bornstein et al. (1987a), the urban and LIS maxima were not separate as in the current results. Individual effects will be clarified in the Run 3 results, when water bodies are not included in the simulation.

UHI accelerations are not apparent at 525 m (Fig. 10), which shows roughness-induced minimum speeds both over the urban area and in the downwind bow. Note that the LIS-induced maximum does not extend to this level, but that the ocean-induced maximum is still present in the area in which the two-dimensional simulations of Bornstein (1975) showed an UHI induced maximum. This point will be further explored in Run 3.

Concurrent vertical velocities at 400 m (Fig. 11) show maximum rising motions over the city (1.75 cm/s) due to its roughness-induced deceleration and in the downwind urban-induced confluence plume. Much of the downward motion surrounding this upward motion is due to offshore acceleration, but some is also due to UHI acceleration, as will be shown in the results from Runs 2 and 3. Note that the smaller domain of Bornstein et al. (1987a) could not show this downwind urban plume. A vertical east to west cross section through Manhattan (Fig. 12) shows that the Δz_0 -linked upward motions are shallower than the downward motions from the combined coastal and UHI accelerations; the subsequent simulations will delineate the contribution from each of these two effects.

Offshore flow persists until 1000 LST, with the stronger offshore confluence area at 50 m (Fig. 13) due to the combination of stronger turning of winds downwind of the city with the beginning of a sea breeze rotation. Note the maximum-vector length has changed from that in Fig. 8 (for clarity). The exact contribution of each of these effects will again be delineated by results from Runs 2 and 3.

The 0600 LST offshore maximum horizontal speed area, however, has now at 1000 LST been converted to an offshore minimum, due to the strengthened confluence region (Fig. 14). Its minimum horizontal speed (around 0.5 m/s) area extends at least to 525 m (Fig. 15), where it is weaker than near the surface. While the 0600 LST roughness-induced minimum speed area over the city at 50 m is no longer present at 1000 LST (Fig. 14), the UHI acceleration is now more clearly developed at this low level. The previous roughness-induced minimum horizontal speed area over the city at 525 m is now replaced by an UHI-induced maximum speed area (Fig. 15).

The concurrent 1000 LST vertical structure of these urban accelerations and coastal deceleration are seen in two east to west cross sections: one 21 km south of the tip of Manhattan (Fig. 16) and the other (more northerly) over Long Island and urban Manhattan (Fig. 17). The southern section shows a split in the elevated center of offshore

maximum speeds at 1020 m due to minimum speeds associated with formation of the sea breeze front, which extends to an elevation of 850 m. This split is not evident in the urban cross section (Fig. 17), as the sea breeze confluence has not yet penetrated this far north.

Sea breeze fronts at 50 m have penetrated inland by 1400 LST from both the Atlantic Ocean and LIS (Fig. 18); the northern LIS breeze was not found in the small domain of Bornstein et al. (1987a). The ocean breeze, the larger and stronger of the two (with a maximum speed of 7.2 m/s), has penetrated 30-35 km into New Jersey in the region south of Staten Island, but has not yet reached the center of NYC. The area of penetration of the southern LIS breeze over northern Long Island (east of the urban center) is more extensive than that of the ocean sea breeze on its southern shore, but its southward penetration is helped in this case by the northwesterly general flow. With a more common southwesterly flow, its southward penetration would be less. The sea breeze confluence is not present at 1020 m (Fig. 19), although minimum speed values do exist along the southern shore of Long Island.

The 1400 LST vertical structure of horizontal wind speed values in an east to west cross section located 21 km south of Manhattan (Fig. 20) shows strong gradients where the opposing flows meet, with the onshore sea breeze undercutting the prevailing offshore flow. The sea breeze front (located at the sloping line of minimum speed) has a maximum depth of about 850 m. Note that the leading inland edge of the marine air looks like a moving gravity head, as indicated by its vertical bulge. This phenomenon has been found in the Tokyo observations of Nakane and Sasano (1986).

The 1400 LST horizontal distribution of vertical velocity at 1400 m (Fig. 21) shows both a narrow band of upward values along the sea breeze front and sinking motion behind it in the marine air. This pattern is associated with the rise of the offshore flow over the inland moving sea breeze front and its subsequent offshore subsidence (Bornstein 1987a).

By 1700 LST (not shown) the ocean breeze flow has penetrated 35 to 40 km inland (past Manhattan and into New Jersey). The LIS breezes have also penetrated southward over most of Long Island and northward into Connecticut. All of the breezes start to retreat by 1900 LST (not shown) as land breezes re-develop; by 2000 LST they have completely dissipated.

b. Run 2

The second simulation does not include NYC urban or super urban grid points. The urban Δz_0 and UHI effects present over the urban area at 50 m in Run 1 at 0600 LST are now thus gone (Fig. 22), resulting in contours that parallel the coastline. With the absence of the Run 1 urban Δz_0 -deceleration of Fig. 10, well defined areas of maximum horizontal speed at the 525 m level (Fig. 23) now exist over the small water bodies NE (i.e., LIS) and SW (i.e., the New York bite) of the City.

The 0600 LST horizontal distribution of vertical velocity at 525 m (not shown) shows neither the near-in nor the previous offshore upward motion areas associated with the urban Δz_0 and confluence effects, respectively. The east to west vertical cross section through the southern part of Manhattan (not shown) also shows a lack of either of these urban influences; only a weak coastal induced vertical velocity field now exists.

Horizontal wind vectors at 1000 LST again show the beginning of an offshore sea breeze rotation at 50 m (Fig. 24), but do not show the urban induced turning that produced the confluence region of Run 1 (Fig. 13). Without urban influences, the maximum speed is now larger than in Run 1 (3.1 vs. 2.8 m/s). The lack of the Run 1 (Fig. 14) confluence-induced U_{\min} at 50 m in the current simulation allows for formation of sea breeze frontal U_{\min} bands along both southern coasts (Fig. 25).

Horizontal wind vectors at 50 m for 1400 LST (Fig. 26) show that the ocean sea breeze has penetrated further inland (by about 10 km) than in Run 1 (Fig. 18) due to the absence of a retarding urban Δz_0 effect. Urban retardation of sea breeze frontal movement over NYC was observed by Bornstein (1987). While the concurrent vertical velocity pattern at 1020 m is similar to that of Run 1, it now, however, reflects the current greater inland frontal penetration (Fig. 27).

c. Run 3

The final simulation investigates urban effects on the prevailing northwesterly flow, without the interacting effects from either the Atlantic Ocean or LIS. The 0600 LST winds at 50 m (Fig. 28) thus show a stronger area of offshore urban-induced confluence, as compared to concurrent Run 1 results (Fig. 8).

The 0600 LST horizontal wind speeds at 50 m (Fig. 29) show a strong downwind offshore urban induced minimum as a result of the confluence. As all water bodies are missing in the simulation, the UHI contribution to the area of maximum horizontal speed can be compared with that of Run 1 (Fig. 9). The UHI alone produces an arc of high speeds centered over the city, but more clearly defined south of the city (due to the asymmetric nature of NYC).

The 0600 LST total horizontal speed at 725 m (Fig. 30) now shows a better defined urban roughness induced minimum of U over the upwind half of the urban area than in Run 1 (Fig. 10); it also shows a maximum speed area downwind of the city. Thus the previous offshore U_{\max} in Run 1 was in fact due to a combination of UHI and coastal accelerations. Note Fig. 30 is located one grid point (or 200 m) above the level shown in Fig. 10, but this difference is not significant, as both effects in the two simulations were visible at both levels (as discussed below).

The 0600 LST horizontal distribution of vertical velocity at 350 m (Fig. 31) exhibits a peak upward magnitude of about 2.5 cm/s associated with the confluence-induced minimum horizontal speed area. Negative values slightly upwind of the urban area are due to UHI accelerations. Note that the absence of the offshore coastal-induced downward motion of Fig. 31 has resulted in a more coherent (and somewhat stronger) urban plume of upward motion oriented more eastward than in Fig. 11. A vertical cross section over the southern part of Manhattan (Fig. 32) shows a similar shallow (680 m) intrusion of upward motion (from the urban roughness) into the UHI-induced downward speed area seen in Run 1 (Fig. 12).

The near-surface flow at 1000 LST (Fig. 33) shows a stronger urban induced confluence (with a lower maximum speed of 2.5 m/s) than with Run 1 (Fig. 13), where the maximum speed was 2.8 m/s. The confluence area appears to arise from the presence of the urban area, as air on both sides of the city is forced around the city and then converges on its downwind side. The presence of the Atlantic Ocean in Run 1 reduced this effect, due to its pre-frontal offshore rotation (Fig. 13). The upwind UHI acceleration and downwind (offshore) confluence deceleration patterns are now clearer both near the surface and aloft (Figs. 34 and 35, respectively), than in the Run 1 results (Figs. 14 and 15, respectively).

5. CONCLUSION

The URBMET urban boundary layer model was improved in the areas of its lateral boundary conditions, stable surface boundary layer formulation, and initialization procedure. Lateral boundary conditions were posed using the concept of "strong" versus "weak" inflow and outflow cases to produce new conditions based, not on the direction of the resultant (large scale plus mesoscale) boundary flow, but only on the direction of the mesoscale forcing at the boundary. A new stable SBL formulation was employed to extend the range into the stable regime for which model calculations could be carried out. Initialization of the model was enhanced to include procedures in which new computer code was tested for formulation, numerical, programming, and/or roundoff errors. In addition, the model domain was expanded both to the south and east from that of Bornstein et al. (1987a).

The model was then used to simulate the time-varying coastal PBL in the NYC area for 9 March 1966. Observational data from this period have been extensively analyzed by Bornstein (1987), because they contained both a well-developed UHI and a sea breeze frontal passage. In addition, a parametric study consisting of two additional simulations sequentially investigated individual effects from the city and local water bodies on the NYC urban coastal environment. Results were compared to the observations summarized in Bornstein (1987), and to results from both the two-dimensional URBMET simulations of Bornstein (1975) and the three-dimensional URBMET simulations of Bornstein et al. (1987a).

Run 1 modeled the effects of both the urban area and local water bodies. The simulated sea breeze front reproduced many of the observed features of the coastal boundary layer flows in NYC, e.g., diurnal variation of offshore and onshore flows and sea breeze frontal penetrations from both the Atlantic Ocean and Long Island Sound. One

surprising result was the deep southward penetration of the LIS front over Long Island. While this penetration was apparently reinforced by the prevailing northwesterly flow, it is a phenomenon that should be further investigated.

In addition, the model reproduced many observed urban impacts on those flows, e.g., Δz_0 deceleration, UHI acceleration, and retardation of the front. Results did not, however, show the wave in the sea breeze front. Observations by Bornstein (1987) have shown that this phenomenon is produced by an urban barrier effect that retards inland movement of the front. Future simulations should include the urban barrier effect via inclusion of urban building heights.

Comparison of the current results with those of Bornstein (1975) shows that the inclusion of lateral variations in the current three-dimensional formulation produces significant changes from the two-dimensional vertical-plane results. Results from the older model showed urban Δz_0 deceleration and UHI acceleration horizontally in line with the general flow direction. The three-dimensional grid of the current simulations showed the deceleration and acceleration areas as side by side. The expanded domain over that used by Bornstein et al. (1987a) revealed a downwind offshore urban induced confluence region not seen in the earlier results.

Run 2 investigated NYC area flows in the absence of urban and super urban grid points. Simulated horizontal wind flow patterns near the surface again showed the early offshore sea breeze rotation, but did not, however, reproduce the urban induced turning that produced the downwind offshore confluence region found in Run 1; wind speeds in this area were thus larger in Run 2. The ocean sea breeze penetrated further inland (by about 10 km) than in Run 1 at 1400 LST, due to the absence of urban Δz_0 induced retardation effects.

Run 3 investigated the influence of the city, without the interacting effects from Long Island Sound and the Atlantic Ocean. With the absence of all water grid points,

UHI induced accelerations produced an arc of high speeds centered over the city, but more clearly defined to the south of the city than to its north.

Results also showed that the offshore U_{\max} of Run 1 was due to a combination of UHI and coastal accelerations. With no water bodies present, a stronger urban turning-induced confluence developed than seen in Run 1. The confluence arose as air on both sides of the city was turned around the city and converged on its downwind side. The presence of the Atlantic Ocean in Run 1 had reduced this effect, due to oceanic inducement of a pre-frontal offshore rotation.

In summary, the improved lateral boundary conditions, stable surface boundary layer formulation, and initialization procedure, as well as its expanded grid domain, have improved the capabilities of the URBMET PBL model to reproduce most of the important features of the NYC urban coastal environment during sea breeze flow conditions. Further important developments in the model formulation should include topography, linkage with time and space varying large scale forcings, and a nested grid capacity. Surface roughness alone cannot reproduce urban barrier effects on sea breeze frontal movement. Nested grids would provide more insight into the location and magnitudes of the urban acceleration and deceleration areas, as well as into the movement and structure of sea breeze fronts. Inclusion of time and space varying large scale forcings would allow for multi-day simulations during periods of changing synoptic conditions.

Future parametric studies should also be conducted to investigate the individual flow field effect resulting from urban surface roughness, heat island processes, and urban barrier effects. Meteorological fields derived from these parametric studies could be used as input for Lagrangian point source, urban passive dispersion, and photochemical air quality models to study the individual effects that these processes have on urban pollution dispersion.

Different prevailing flow directions should be simulated to understand the structure of the polluted NYC urban boundary layer under sea breeze and non-sea breeze conditions. The asymmetry of the city and the complex shoreline of the area will undoubtedly produce results differing significantly from those of the present study. A limitation of such studies may be a lack of intensive field data for comparison to simulated values.

REFERENCES

- Bornstein, R. D., 1975: The two-dimensional URBMET urban boundary layer model. *J. Appl. Meteor.*, **14**, 1459-1477.
- Bornstein, R. D., 1987: Mean diurnal circulation and thermodynamic evolution of urban boundary layers. In *Modeling the Urban Boundary Layer*, American Meteor. Soc., Boston, MA, 53-93.
- Bornstein, R. D., and A. D. Robock, 1976: Effects of variable and unequal time steps for advective and diffusive processes in simulations of the urban boundary layer. *Mon. Wea. Rev.*, **104**, 260-267.
- Bornstein, R. D., S. Klotz, U. Pechinger, R. Salvador, R. Street, L. J. Shieh, F. Ludwig, and R. Miller, 1986: Application of linked three-dimensional PBL and dispersion models to New York City. In *Air Pollution Modeling and its Application V*, Plenum Press, New York, 543-564.
- Bornstein, R. D., S. Klotz, U. Pechinger, R. Street, and R. Miller, 1987a: Modeling the polluted coastal urban environment. Vol. I: The PBL model. EPRI Final Report EA 5091 for Project 1630-13, 175 pp.
- Bornstein, R. D., U. Pechinger, R. Salvador, L. J. Shieh, and F. Ludwig, 1987b: Modeling the polluted coastal urban environment. Vol. II: The dispersion model. EPRI Final Report EA 5091 for Project 1630-13, 123 pp.
- Bornstein, R. D., P. Thunis, and G. Schayes, 1993: Simulation of urban barrier effects on polluted urban boundary layers using the three-dimensional URBMET/TVM model with urban topography - new results from NYC. In *Air Pollution, Computational Mechanics Publications*, Southampton, UK, 15-34.
- Bornstein, R. D., P. Thunis, and G. Schayes, 1995b: The Topographic Vorticity-mode Mesoscale- β (TVM) model: Part II-Application to the Fos Experiment. Accepted, *J. Appl. Meteor.*
- Burden, R. L., and J. D. Faires, 1985: Numerical Analysis. PWS Publishers, 676 pp.
- Businger, J. A., J. C. Wyngaard, Y. Izumi, and E. F. Bradley, 1971: Flux-profile relationships in the atmospheric surface layer. *J. Atmos. Sci.*, **28**, 181-189.
- Carson, D. J., and P. J. R. Richards, 1978: Modeling surface turbulent fluxes in stable conditions. *Bound.-Layer Meteor.*, **14**, 67-81.

- Clark, T. L., 1977: A small-scale dynamic model using a terrain-following coordinate transformation. *J. Comput. Phys.*, **24**, 186-215.
- Clarke, R. H., 1970a: Observational studies in the atmospheric boundary layer. *Quart. J. Roy. Meteor. Soc.*, **96**, 91-114.
- Delvosalle, C., J. M. Levert, F. Benjelloun, G. Schayes, B. Moyaux, F. Runday, E. Everbecq, T. Bourouag, and J. P. Dzisiak, 1993: Major industrial hazards: The SEVEX Project. In *Air Pollution Modeling and its Application X*, Plenum Press, New York, 357-365.
- Dieterle, D., 1979: Simulation of urban surface energy balance, including effects of anthropogenic heat production. M. S. Thesis, Dept. of Meteor., San Jose State Univ., 65 pp.
- Draxler, R. R., 1986: Simulated and observed influence of the nocturnal urban heat island on the local wind field. *J. Appl. Meteor.*, **25**, 1125-1133.
- Eichorn, J., R. Schrodin, and W. Zdunkowski, 1988: Three-dimensional numerical simulations of the urban climate. *Beitr. Phys. Atmosph.*, **61**, 187-203.
- Estoque, M. A., 1961: A theoretical investigation of the sea breeze. *Quart. J. Roy. Meteor. Soc.*, **87**, 136-46.
- Flassak, T., M. Wortmann, and N. Moussiopoulos, 1992: Monitoring and Modeling in the Mesoscale. Univ. of Thessalonki Report, Greece, 155-166.
- Fruehauf, G. L., 1991: Numerical simulation of PBL depth during subsidence inversion conditions. M. S. Thesis, Dept. of Meteor., San Jose State Univ., 81 pp.
- Goldberg, D., 1991: What every computer scientist should know about floating-point arithmetic. *ACM Computing Surveys*, **23**, 5-48.
- Grossi, P., J. M. Giovannoni, and A. G. Russel, 1995: Intercomparison of meteorological models applied to the Athens area, and their effects on photochemical pollutant concentrations and transport. Submitted to *J. Appl. Meteor.*
- Hicks, B. B., 1976: Wind profile relationships from the "Wangara" Experiment. *Quart. J. Roy. Meteor. Soc.*, **102**, 535-551.
- Hjelmfelt, M. R., 1982: Numerical simulation of the effects of St. Louis on the mesoscale boundary-layer airflow and vertical air motion: Simulations of urban vs. non-urban effects. *J. Appl. Meteor.*, **21**, 1239-1257.

- Högström, U., 1988: Non-dimensional wind and temperature profiles in the atmospheric surface layer: a re-evaluation. *Bound.-Layer Meteor.*, **42**, 55-78.
- Holtslag, A. A., and H. A. R. DeBruin, 1988: Applied modeling of the nighttime surface energy balance over land. *J. Appl. Meteor.*, **27**, 689-704.
- Kimura, F., 1985: A numerical simulation of local winds and photochemical air pollution (II): Application to the Kanto Plain. *J. Meteor. Soc. Japan*, **63**, 923-936.
- Kimura, F., 1989: Heat flux on mixtures of different land-use surface: Test of a new parameterization scheme. *J. Meteor. Soc. Japan*, **67**, 401-409.
- Kimura, F., and S. Takahashi, 1990: Climatic effects of land reclamation in Tokyo Bay-Numerical experiment. *Energy and Building*, **15-16**, 147-156.
- Kimura, F., and S. Takahashi, 1991: The effects of land-use and anthropogenic heating on the surface temperature in the Tokyo Metropolitan area: A numerical experiment. *Atmos. Environ.*, **25B**, 155-164.
- Martien, P., 1991: Models of urban climate: Description and applications to the study of energy use in buildings. M. S. Thesis, Dept of Mechanical Engineering, Univ. of Calif. at Berkeley.
- McPherson, R. D., 1970: A numerical study of the effect of a coastal irregularity on the sea breeze. *J. Appl. Meteor.*, **9**, 767-777.
- Monin, A. S., and A. M. Obukhov, 1954: Basic regularity in turbulent mixing in the surface layer of the atmosphere. *Tr. Akad. Nauk SSR, Geofiz. Inst.*, **24**, 1963-1987.
- Nakane, H., and Y. Sanano, 1986: Structure of a sea breeze front revealed by a scanning Lidar observation. *J. Meteor. Soc. Japan*, **64**, 787-792.
- Neumann, J., and Y. Mahrer, 1971: A theoretical study of the land and sea breeze circulations. *J. Atmos. Sci.*, **28**, 532-542.
- O'Brien, J., 1970: On the vertical structure of the eddy exchange coefficient in the planetary boundary layer. *J. Atmos. Sci.*, **27**, 1213-1215.
- Pechinger, U., and P. Seibert, 1990: Observations and simulations with linked numerical PBL and air pollution models and a Gaussian model under low wind speed conditions: Study of the urban-industrial Linz area. *Il Nuovo Cimento*, **13**, 903-915.

- Piekle, R., 1984: *Mesoscale Meteorological Modeling*. Academic Press, 468 pp.
- Rao, S. T., G. Sistla, J. Y. Ku, N. Zhou, W. Hao, P. Thunis, R. D. Bornstein, and F. Freedman, 1993: Sensitivity of the UAM to a spatially varying mixing height profile. Presented at AWMA Specialty Conf. on Regional Photochem. Measurement and Modeling Studies, San Diego, CA, 8-12 Nov.
- Reichenbacher, W., and R. D. Bornstein, 1979: Experiments with time and space varying upper boundary conditions in a PBL model. *Preprint Volume, 4th AMS Symposium on Turbulence, Diffusion and Air Pollution*, Reno, Nevada, 483-490.
- Russell, A. G., K. McCue, and G. Cass, 1988: Mathematical modeling of the formation of nitrogen-containing pollutants. *Environ. Sci. and Tech.*, **22**, 263-271.
- Santhanam, K., 1980: One-dimensional simulation of temperature and moisture in atmospheric and soil layers. M. S. Thesis, Dept. of Meteor., San Jose State Univ., 89 pp.
- Schayes, G., and P. Thunis, 1990: A three-dimensional mesoscale model in vorticity mode. Report No. 60, Institut d'Astronomie, Catholic Univ., Louvain-la-Neuve, Belgium, 43 pp.
- Schayes, G., and B. Moyaux, 1992: Project SEVEX (Phase III). Les industries à risques majeurs en Région Wallone, Rapport final (Vol. 3). Institut d'Astronomie et de Géophysique G. Lemaître, UCL, Louvain-la-Neuve, 95 pp.
- Schayes, G., J. Smits, P. Thunis, and L. Lesage, 1990: The SEVEX project, an integrated dispersion and contamination calculation for complex terrain and accidental releases. *Air Pollution Modeling and its Applications VIII*, Plenum Press, 643-648.
- Schayes, G., P. Thunis, and R. D. Bornstein, 1995: The Topographic Vorticity-mode Mesoscale- β (TVM) Model: Part I-Formulation. Accepted, *J. Appl. Meteor.*
- Seaman, N., L. L. Ludwig, E. G. Donall, T. T. Warner, and C. M. Bhumralkar, 1989: Numerical studies of urban planetary boundary-layer structure under realistic synoptic conditions. *J. Appl. Meteor.*, **28**, 760-781.
- Shir, C., and L. J. Shieh, 1974: A generalized air pollution model and its application to the study of sulfur dioxide distributions in the St. Louis metropolitan area. *J. Appl. Meteor.*, **13**, 185-204.
- Shir, C., and R. D. Bornstein, 1977: Eddy exchange coefficients in numerical models of the planetary boundary layer. *Bound.-Layer Meteor.*, **11**, 171-185.

- Sistla, G., N. Zhou, W. Hao, J. Y. Ku, S. T. Rao, R. D. Bornstein, F. Freedman, and P. Thunis, 1995: Sensitivity of UAM predicted ozone concentrations to meteorological input and emissions control strategies. Accepted, *Atmos. Environ.*
- Takano, K., 1983: Three-dimensional numerical modeling of the land and sea breezes and the urban heat island in the Kanto Plain. Ph. D. Dissertation, Dept. of Atmospheric Sciences, UCLA, 65 pp.
- Thunis, P., 1995: Formulation and evaluation of a nonhydrostatic vorticity-mode mesoscale model. Ph. D. Dissertation, Inst. d'Astronomie et de Géophysique, Univ. Catholique de Louvain-la-Neuve, 116 pp.
- Thunis, P., and R. D. Bornstein, 1995: Hierarchy of assumptions and equations for deep and shallow mesoscale flows. Accepted, *J. Atmos. Sci.*
- Tripoli, G., 1992: A nonhydrostatic mesoscale model designed to simulate scale interaction. *Mon. Wea. Rev.*, **120**, 1323-1359.
- Tripoli, G., and W. R. Cotton, 1982: The Colorado State University three-dimensional cloud/mesoscale model-1982: Part I: General theoretical framework and sensitivity experiments. *J. Research Atmos.*, **3**, 185-219.
- Vukovich, F. M., J. W. Dunn III, and B. W. Crissman, 1976: A theoretical study of the St. Louis heat island: The wind and temperature distribution. *J Appl. Meteor.*, **15**, 417-440.
- Vukovich, F. M., and J. W. Dunn, 1978: A theoretical study of the St. Louis heat island: Some parameter variations. *J Appl. Meteor.*, **17**, 1585-1594.
- Vukovich, F. M., W. J. King, J. W. Dunn III, and J. J. B. Worth, 1979: Observations and simulations of the diurnal variation of the urban heat island circulation and associated variations of the ozone distribution: A case study. *J. Appl. Meteor.*, **18**, 836-854.
- Vukovich, F. M., and W. J. King, 1980: : A theoretical study of the St. Louis heat island: Comparisons between observed data and simulation results on the urban heat island circulation. *J. Appl. Meteor.*, **19**, 761-770.
- Webb, E. K., 1970: Profile relationships: the log-linear range, and extension to strong stability. *Quart. J. Roy. Meteor. Soc.*, **96**, 67-90.

APPENDIX A: List of Symbols

Roman letters

A	dummy parameter
A^*	surface albedo
A_t	constant in equation for advection time step
a_T	Related to half amplitude of prescribed surface temperature curve
B	base of a real number in floating point form
C	soil heat capacity
c	Priestly mixed convection SBL constant
c_p	specific heat of air
D_t	constant in equation for diffusion time step
d	decimal number in floating point general representation
d_g	daily degree day value
dd	geostrophic wind direction
e	exponent in representation of a real number
F	flux quantity
f	Coriolis parameter
g	acceleration due to gravity
h_s	SBL depth
K	vertical eddy transfer coefficient
K_H	horizontal eddy transfer coefficient
K_{int}	vertical eddy diffusivity in Ekman spiral calculation
K_{max}	maximum allowable vertical eddy diffusivity
K_{min}	minimum allowable vertical eddy diffusivity

k_0	von Kármán constant
L	Monin-Obukhov length
L_E	latent heat of vaporization (at 20 °C)
ℓ	Prandtl turbulent mixing length
P	precision of a real number in floating point form
p	atmospheric pressure
Q_N	net radiation
q	specific humidity
R_d	dry air gas constant
R_w	gas constant of water
R_∞	solar constant
Ri	Richardson number
Ri_C	critical Richardson number at transition from turbulent to laminar flow
Ri_t	Richardson number at transition from forced to mixed convection
Ri_Δ	finite-differenced Richardson number
T	atmospheric temperature
T_0	surface temperature
t	time
t_A	advection time step
t_D	diffusion time step
U	horizontal wind speed
u, v, w	component of wind in x, y, and z-direction, respectively
V	wind speed
x, y, z	E-W, N-S, and vertical coordinates, respectively
z_d	zero-plane displacement

z_0 aerodynamic roughness length

Greek letters

α^* constant in equation for soil moisture potential

β constant in Monin-Obukhov stability function

β^* constant in equation for soil moisture potential

$\beta_1, \beta_2, \beta_3, \beta_4$ constants in stability function equation (0.7, 0.75, 5.0, and 0.35)

Γ dry adiabatic cooling rate

γ_h, γ_m constants in Businger stability function

Δ interval for finite-difference calculation

$\Delta x, \Delta y, \Delta z$ grid intervals

ϵ_0 surface emissivity

θ potential temperature

λ surface heat conductivity

ξ, ζ, ν x, y, and z-components of relative vorticity, respectively

Π longitude

ρ density

ρ_a volume averaged atmospheric density

ρ_w density of water

σ Stefan-Boltzman constant

$\bar{\tau}$ free atmosphere optical thickness

Φ latitude

ϕ, ψ x and y-component of stream function, respectively

ϕ^* nondimensional atmospheric stability function

Ψ stream function

Ψ_m^*	integrated stability function
Ω	relative vorticity
ω_r	optical depth of water vapor above PBL

Superscripts

$\vec{()}$	vector quantity
$\overline{()}$	averaged quantity

Subscripts

$()_A$	advective quantity
$()_a$	constant volume average
$()_C$	critical stability transition quantity
$()_D$	diffusive quantity
$()_E$	eastern-most grid interval
$()_g$	geostrophic
$()_H$	horizontal
$()_h$	heat
$()_i$	sequential index
$()_{IN}$	inflow boundary value
$()_M$	mesoscale
$()_m$	momentum
$()_n$	synoptic
$()_{OUT}$	outflow boundary value
$()_p$	grid averaged value at an arbitrary point

$()_q$	atmospheric moisture
$()_w$	western-most grid interval
$()_*$	friction scale
$()_0$	surface value

APPENDIX B: Extended Precision Registers

Bit Position	$(1/2)^n$	Value
1	$(1/2)^0$	1.0
2	$(1/2)^1$	0.5
3	$(1/2)^2$	0.25
4	$(1/2)^3$	0.125
5	$(1/2)^4$	0.0625
6	$(1/2)^5$	0.03125
7	$(1/2)^6$	0.015625
8	$(1/2)^7$	0.0078125
9	$(1/2)^8$	0.00390625
10	$(1/2)^9$	0.001953125
11	$(1/2)^{10}$	0.0009765625
12	$(1/2)^{11}$	0.00048828125

Table 1

Boundary Condition	Advection	Diffusion	Boussinesq term
Inflow			
Old closed	is zeroed	is zeroed	is zero
New closed	is zeroed	is zeroed	is zero
Advantage:	neither	neither	neither
Outflow			
Old closed	is zeroed (overspecified)	is zeroed	is zero (overspecified)
New quasi open	no condition	is zeroed	no condition
Advantage:	new condition	neither	new condition

Table 2

Boundary	Advection	Diffusion	w(z)
Inflow corner	zero x- and y-advection	zero x- and y-diffusion	zero
East-west inflow	zero y-advection	zero y-diffusion	from $\partial u/\partial x$ only
North-south inflow	zero x-advection	zero x-diffusion	from $\partial v/\partial y$ only
Outflow corner	3-D advection	zero x- and y-diffusion	from $\partial u/\partial x$ and $\partial v/\partial y$
East-west outflow	3-D advection	zero y-diffusion	from $\partial u/\partial x$ and $\partial v/\partial y$
North-south outflow	3-D advection	zero x-diffusion	from $\partial u/\partial x$ and $\partial v/\partial y$
Northeast transition corner	zero y-advection	zero x- and y-diffusion	from $\partial u/\partial x$ only
Southwest transition corner	zero x-advection	zero x- and y-diffusion	from $\partial v/\partial y$ only

	0.0	0.5	1.0	6.0	10.0
Webb (1970)		$\phi^* = 1 + 5.2 \left(\frac{z}{L}\right)$	$\phi^* = 1 + \left(\frac{z}{L}\right)$		
Clark (1970a)		$\phi^* = \frac{1 + 5 \left(\frac{z}{L}\right)}{1 + 0.0079 \left(\frac{z}{L}\right) \left(1 + 5 \left(\frac{z}{L}\right)\right)}$		$\phi^* = \frac{1 + 5}{1 + 0.0079 (1 + 5) \left(\frac{z}{L}\right)}$	
Businger et al. (1971)			$\phi_m^* = 1.0 + 4.7 \left(\frac{z}{L}\right)$ $\phi_h^* = 0.74 + 4.7 \left(\frac{z}{L}\right)$		
Carson and Richards (1978)		$\phi^* = 1 + 5 \left(\frac{z}{L}\right)$		$\phi^* = 8 - 4.25 \left(\frac{z}{L}\right)^{-1} + \left(\frac{z}{L}\right)^{-2}$	$\phi^* = 0.76 \left(\frac{z}{L}\right)$
Hogstrom (1988)		$\phi_m^* = 1 + 6 \left(\frac{z}{L}\right)$ $\phi_h^* = 1 + 7.8 \left(\frac{z}{L}\right)$			
Holslag and DeBruin (1988)		$\phi^* = 1 + 0.75 \frac{z}{L} + 0.75 \frac{z}{L} \left(1 + 5.0 - 0.35 \frac{z}{L}\right) \exp\left(-0.35 \frac{z}{L}\right)$			

Table 3

Table 4

Grid Index	x (km)	y (km)	z (m)
1	-67.5	-52.5	0.0
2	-49.5	-37.5	25.0
3	-34.5	-25.5	50.0
4	-22.5	-16.5	75.0
5	-13.5	-10.5	100.0
6	-7.5	-7.5	150.0
7	-4.5	-4.5	200.0
8	-1.5	-1.5	250.0
9	1.5	1.5	300.0
10	4.5	4.5	350.0
11	7.5	7.5	400.0
12	13.5	10.5	525.0
13	22.5	16.5	725.0
14	34.5	25.5	1020.0
15	49.5	37.5	1400.0

Table 5

Land type	A*	ϵ_0	λ $\left(\frac{\text{cal}}{\text{cm s}^\circ\text{C}}\right)$	C $\left(\frac{10^{-3}\text{cal}}{\text{cm}^3^\circ\text{C}}\right)$	z_0 (cm)	z_d (cm)
water	0.09	0.93	0.0014	1.00	0.1	0.0
rural	0.20	0.88	0.0023	0.45	108.0	0.0
urban	0.25	0.88	0.0022	0.40	250.0	600.0
super-urban	0.26	0.86	0.0024	0.42	400.0	600.0

Table 6

c_p	$1.0 \times 10^7 \text{ erg g}^{-1} \text{ K}^{-1}$
g	981 cm s^{-2}
k_0	0.4
L_E	573 cal g^{-1}
R_d	$2.87 \times 10^6 \text{ erg g}^{-1} \text{ K}^{-1}$
R_w	$4.62 \times 10^6 \text{ erg g}^{-1} \text{ K}^{-1}$
R_∞	$2.58 \times 10^4 \text{ erg cm}^2 \text{ s}^{-1}$
α^*	0.398
β	0.03
β^*	4.4
γ_h	1.2
γ_m	1.93
Γ	$9.8 \times 10^{-5} \text{ K cm}^{-1}$
π	3.14
ρ_c	$1.23 \times 10^{-3} \text{ g cm}^{-3}$
ρ_w	1 g cm^{-3}
σ	$5.67 \times 10^{-5} \text{ erg cm}^{-2} \text{ K}^{-4} \text{ s}^{-1}$
ω_r	1.2 cm

Table 7

A_t	0.6
a_T	14.0 K
c	3.7
D_t	0.75
d_g	5.0 °C
dd	330°
h_s	2.5×10^3 cm
K_H	1.0×10^8 cm ² s ⁻¹
K_{int}	3.0×10^4 cm s ⁻²
K_{max}	2.0×10^6 cm ² s ⁻¹
K_{min}	1000.0
q_a	0.001 g H ₂ O/ g air
Ri_{max}	33.3
Ri_{min}	-0.95
Ri_t	-4.76
T_a	286.0 K
T_0	286.0 K
$(t_D)_{max}$	20
$(t_A)_{max}$	999999
U_g	300.0 cm s ⁻¹
U_{min}	1.0×10^{-6} cm s ⁻¹
$(\Delta t_D)_{min}$	0.5 s
x, y, z	Table 4
z_0	Table 5
$\bar{\tau}$	0.22
Φ	40.75°
Π	74.00°

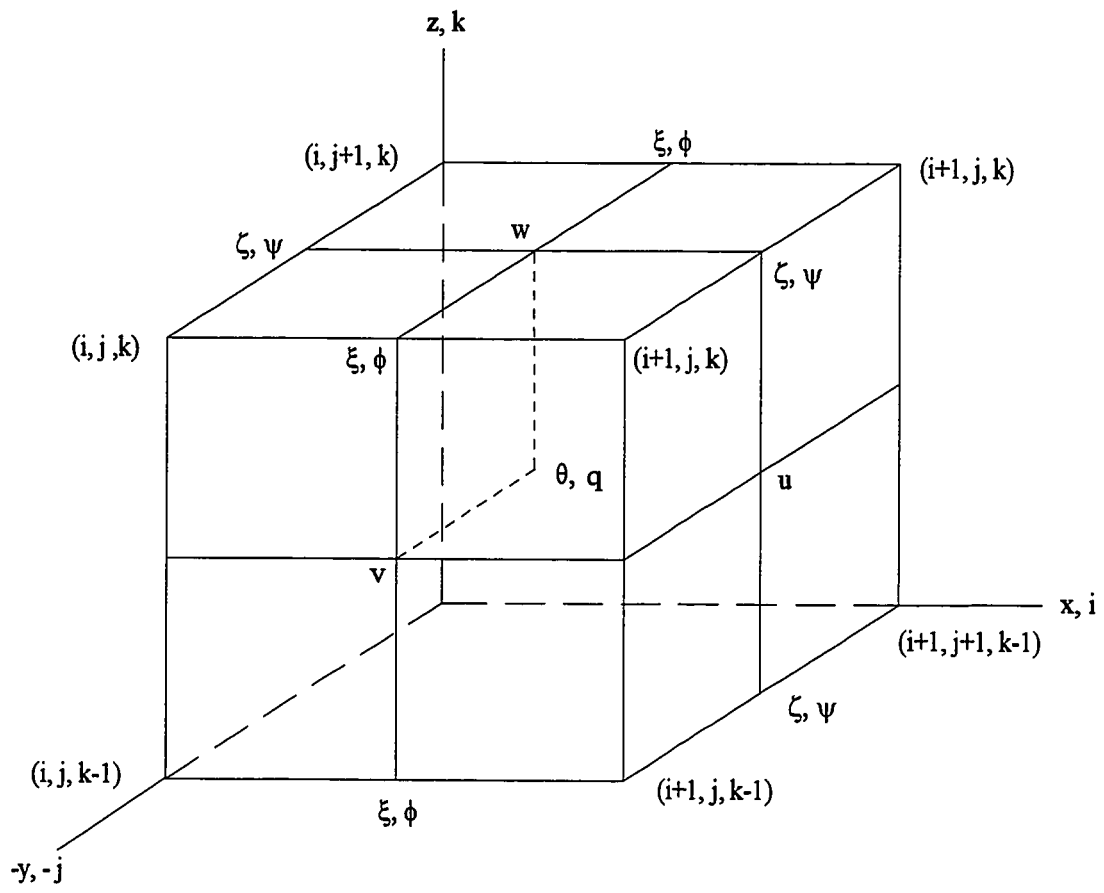


Fig. 1

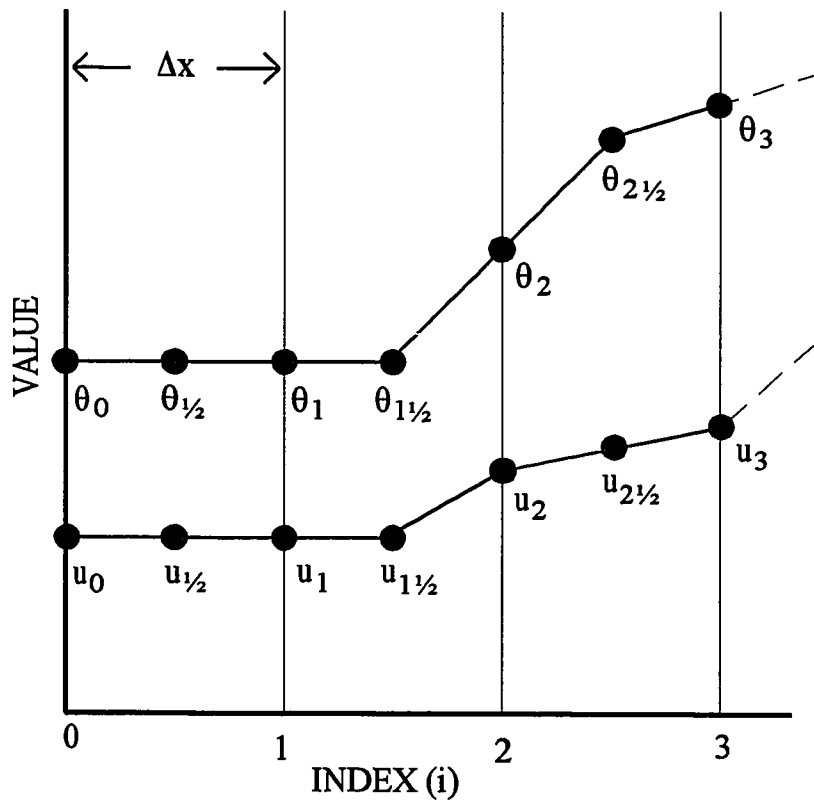


Fig. 2

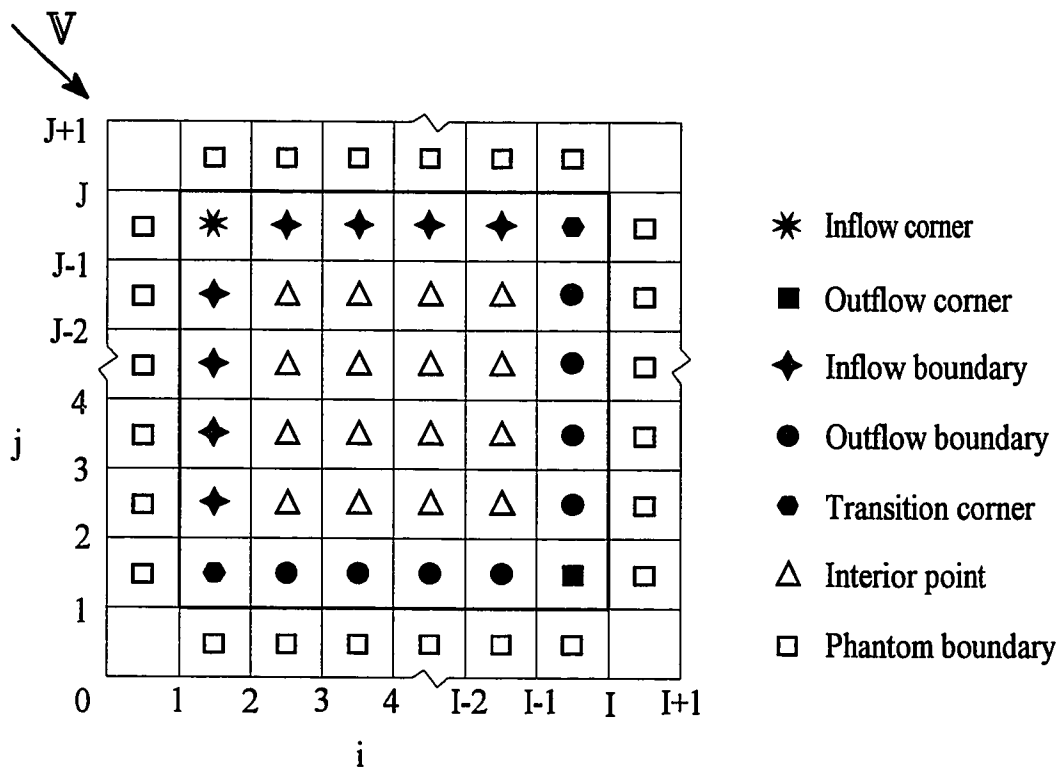


Fig. 3

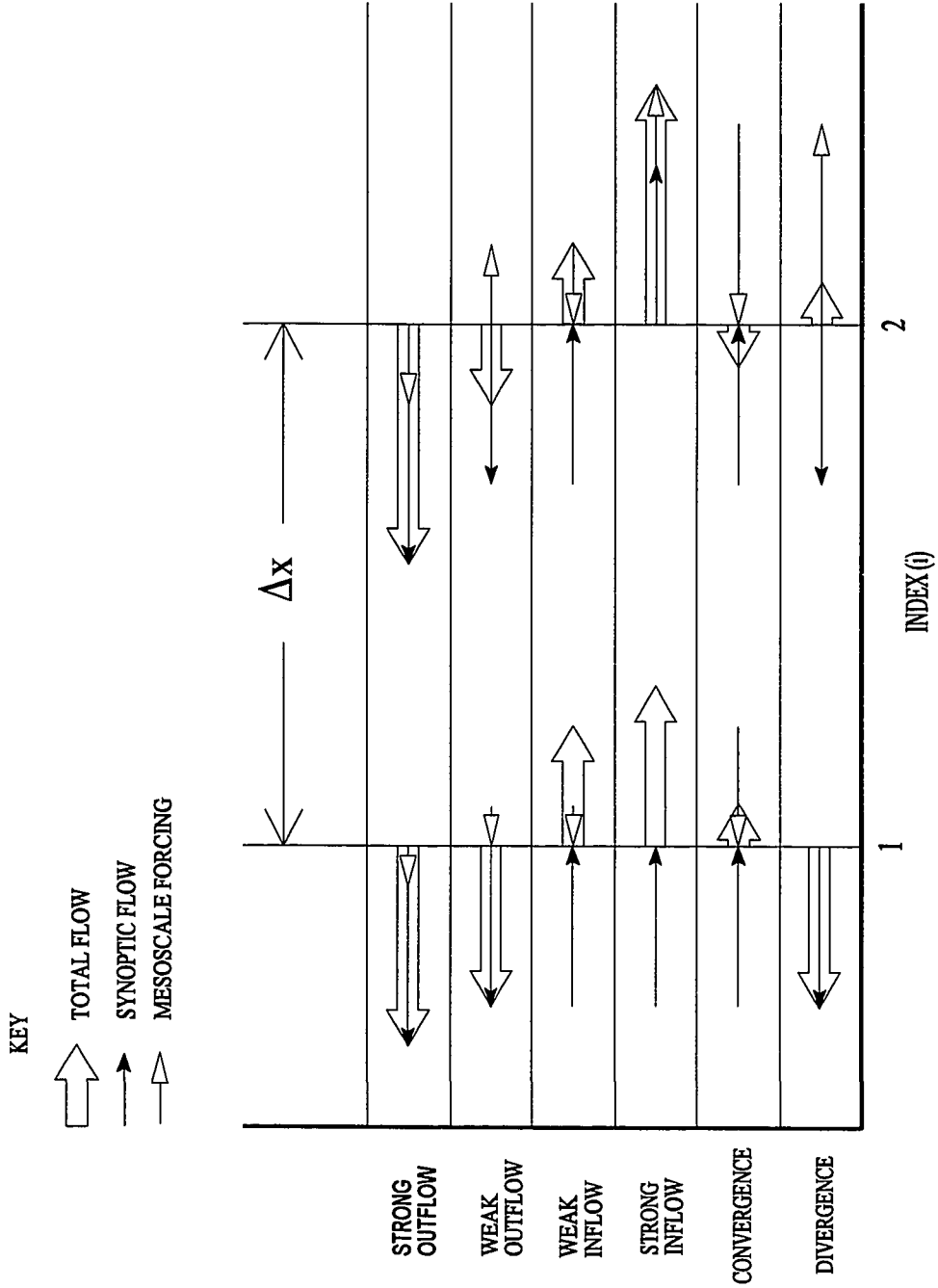


Fig 4

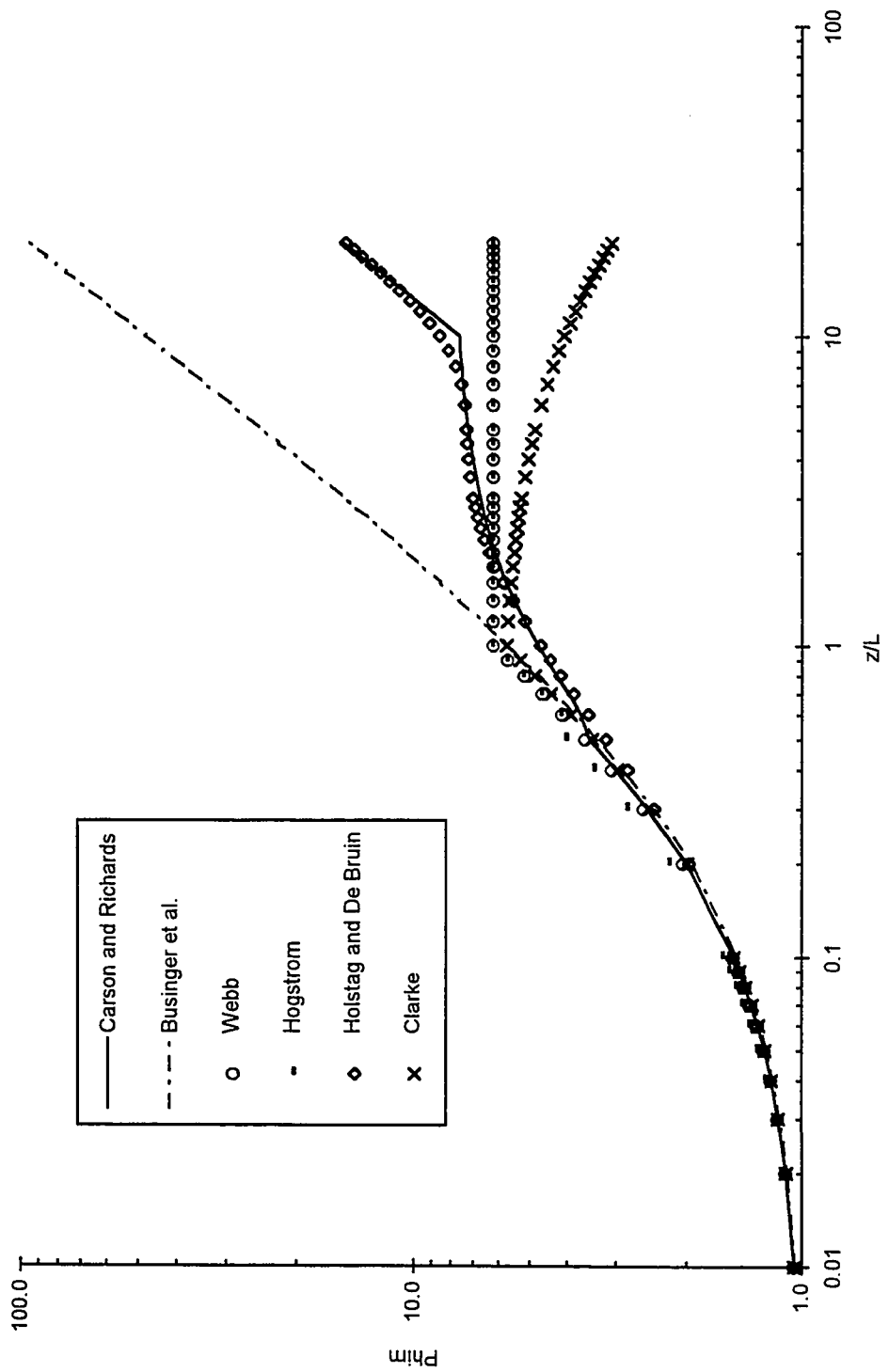


Fig. 5

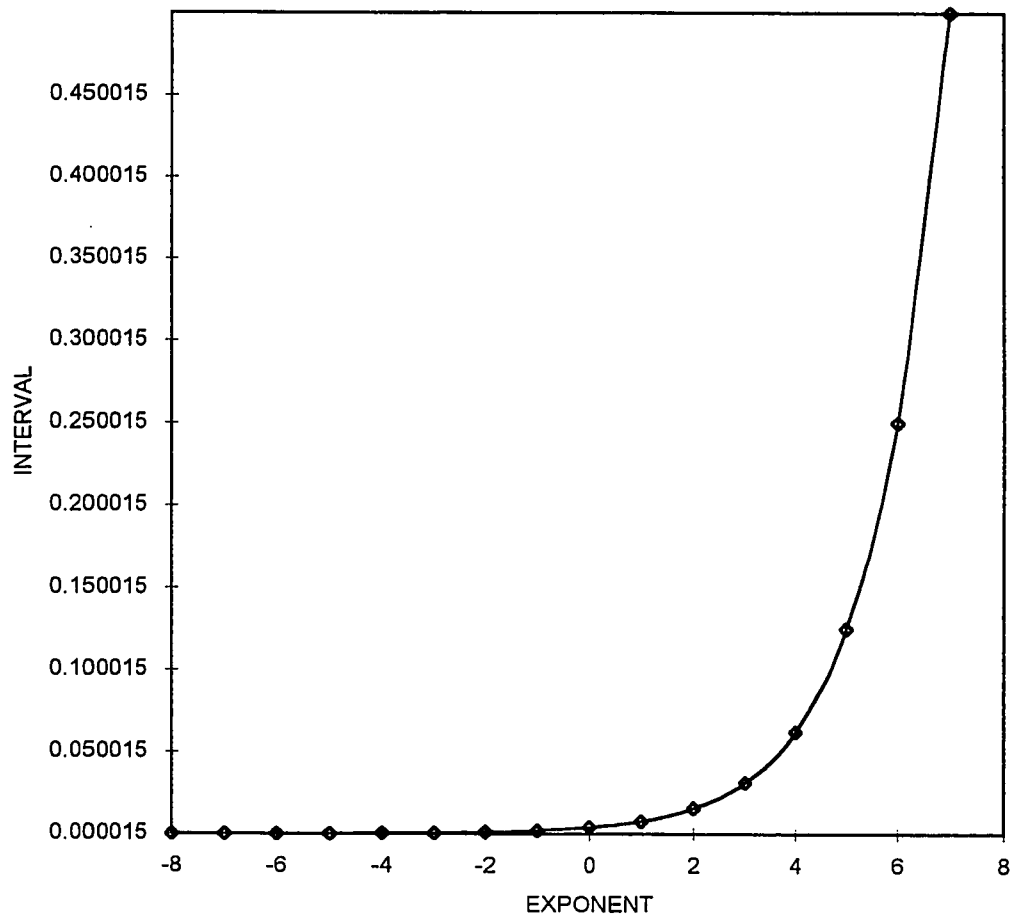


Fig. 6

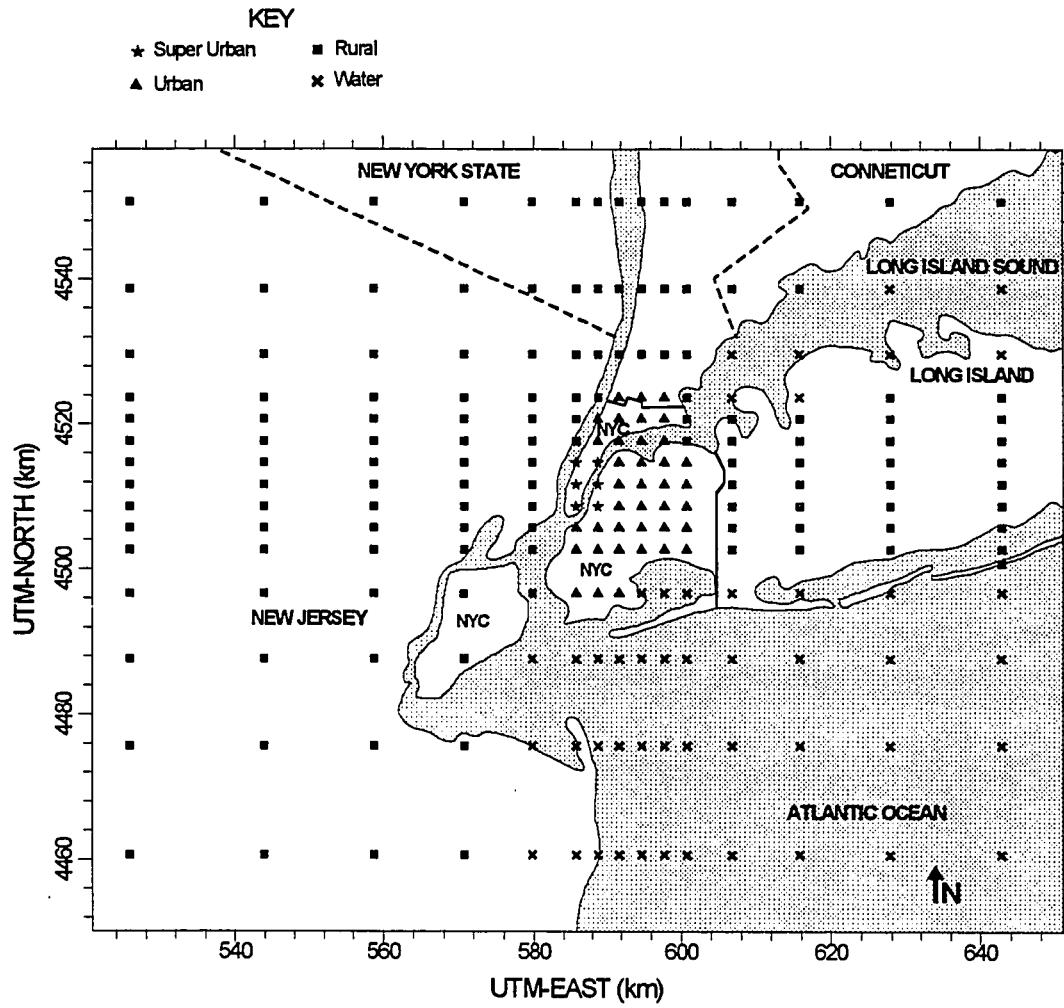


Fig. 7

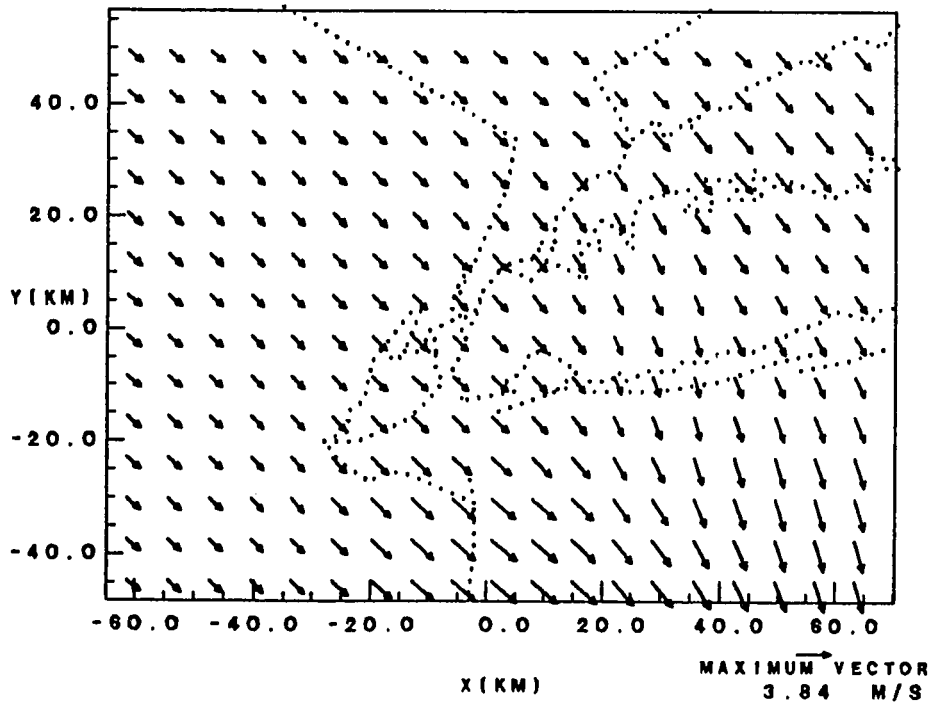


Fig. 8

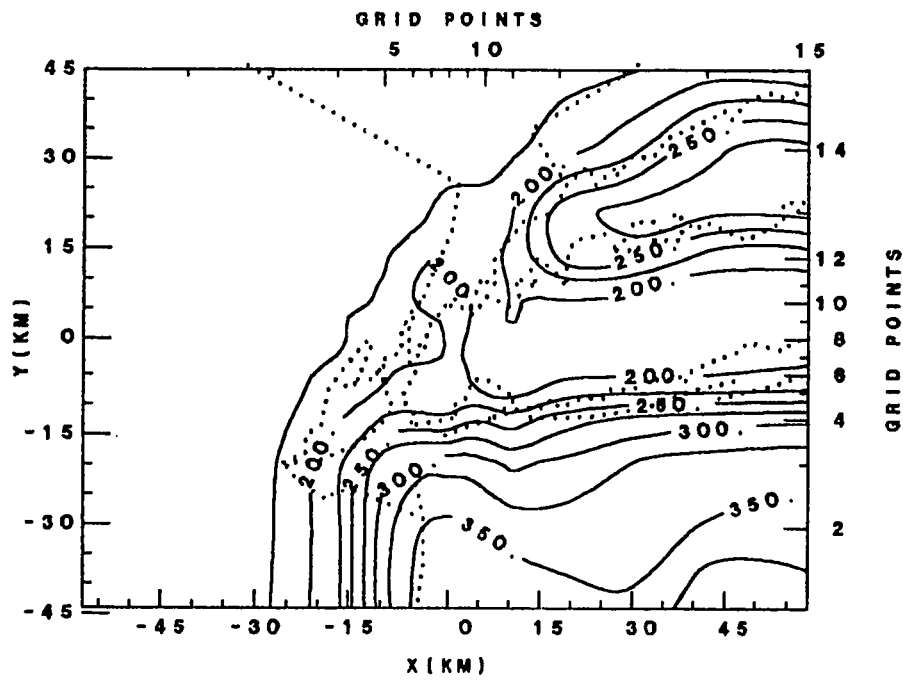


Fig. 9

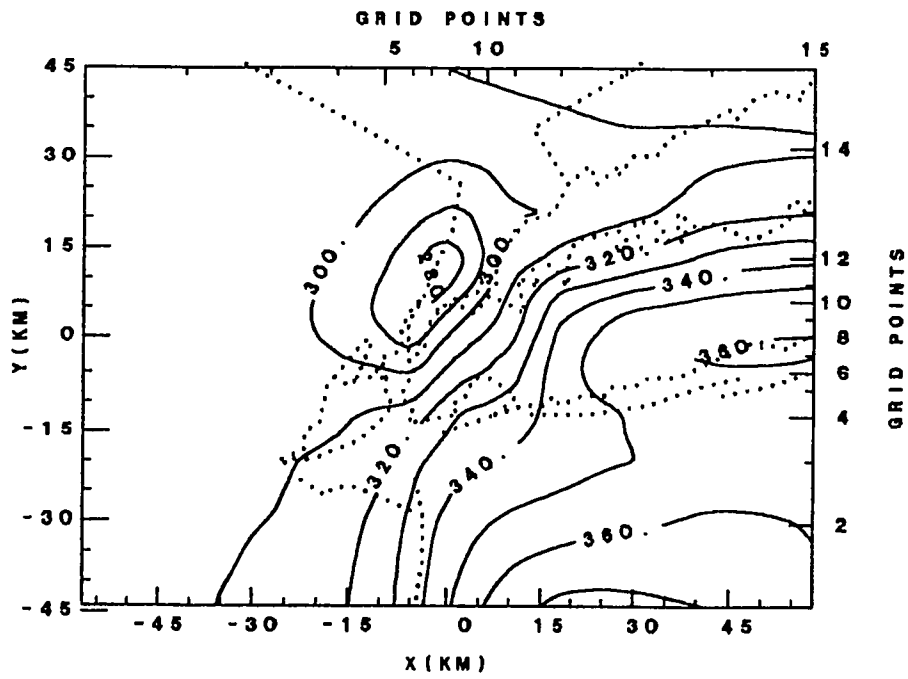


Fig. 10

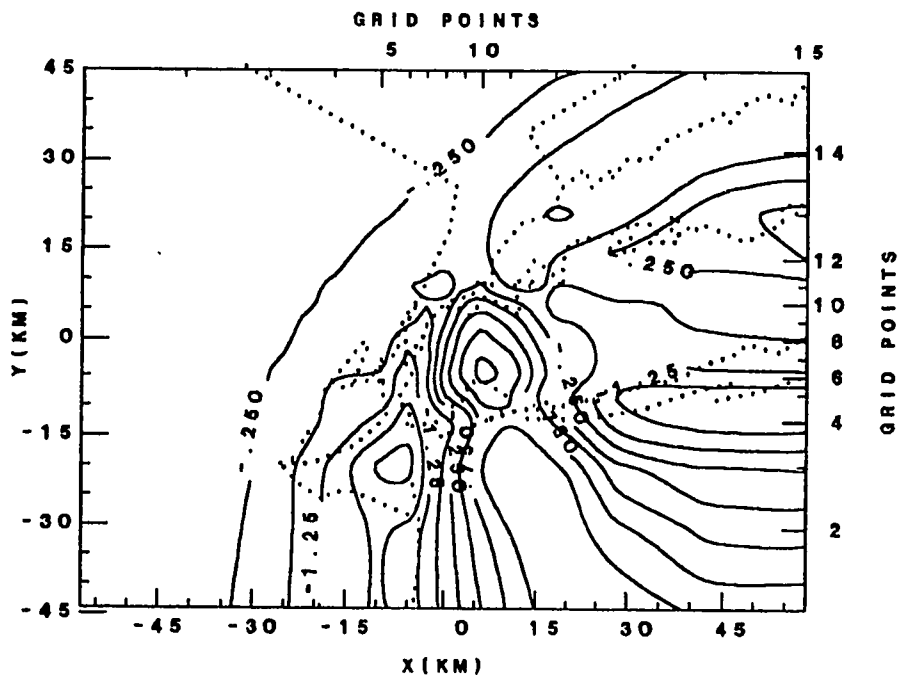


Fig. 11

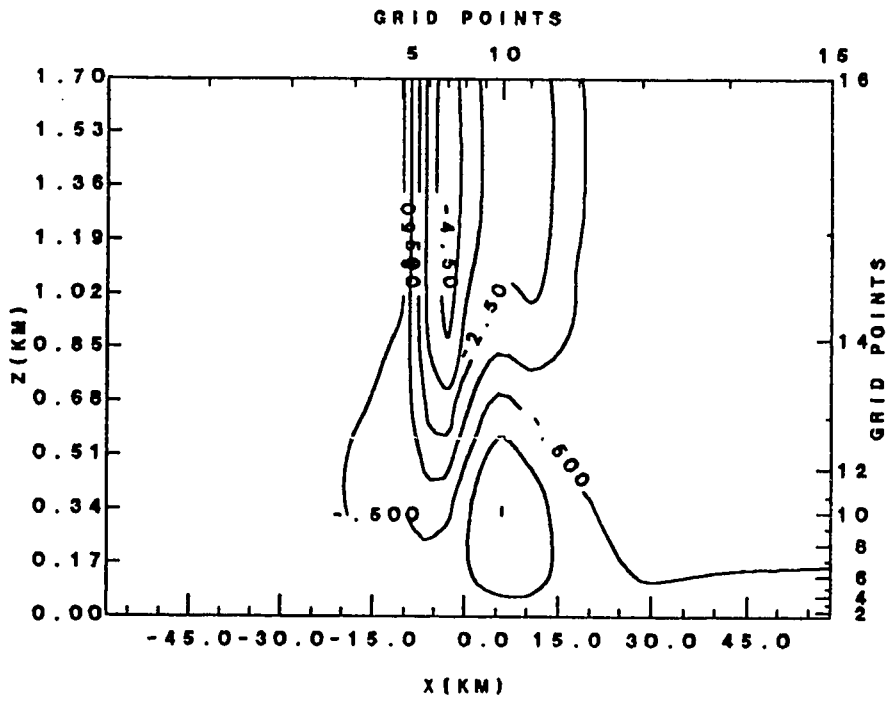


Fig. 12

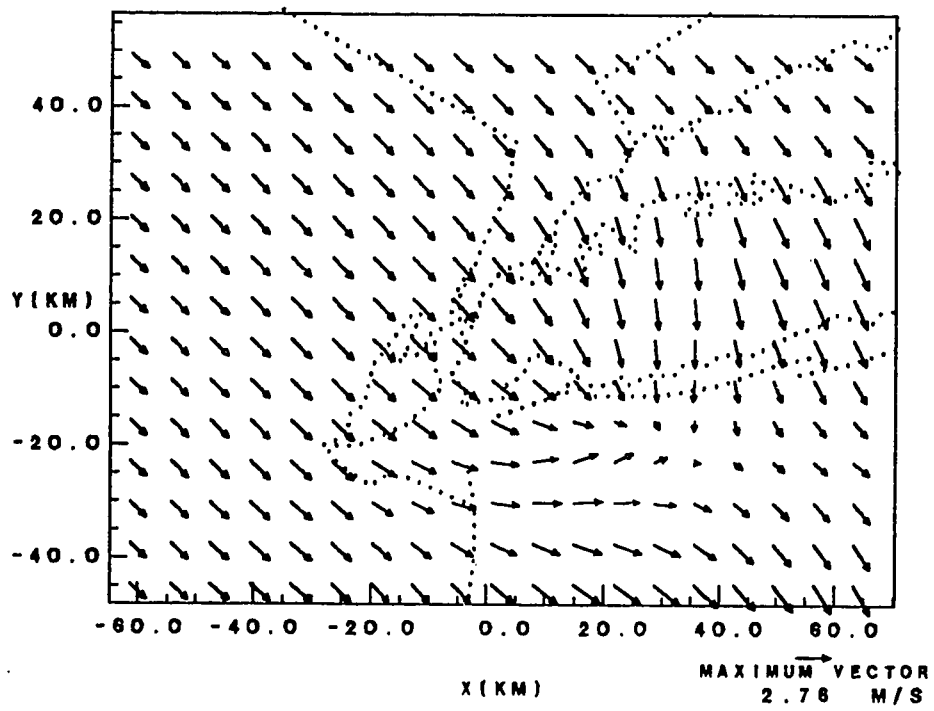


Fig. 13

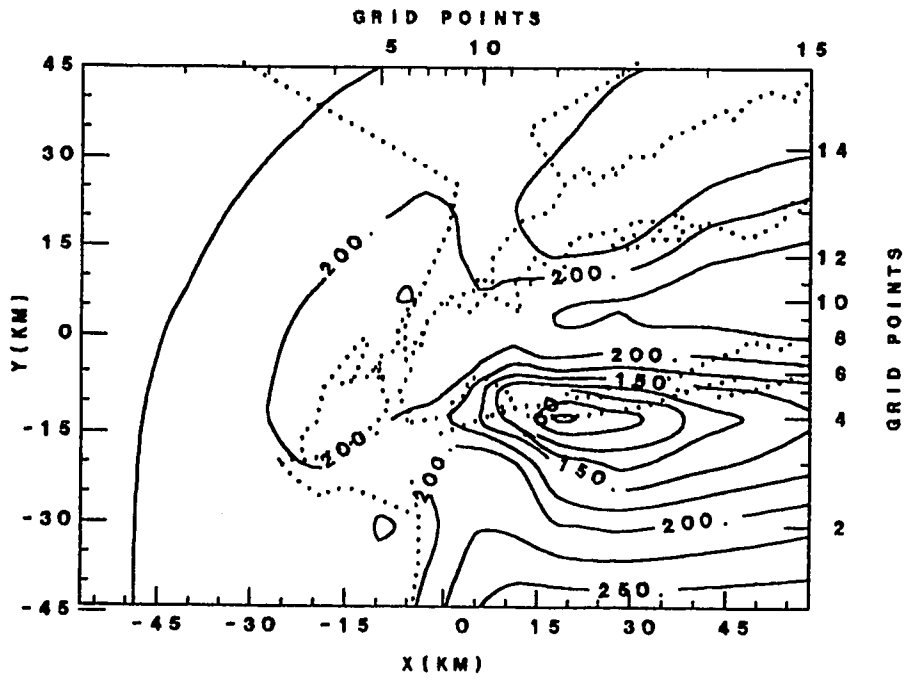


Fig. 14

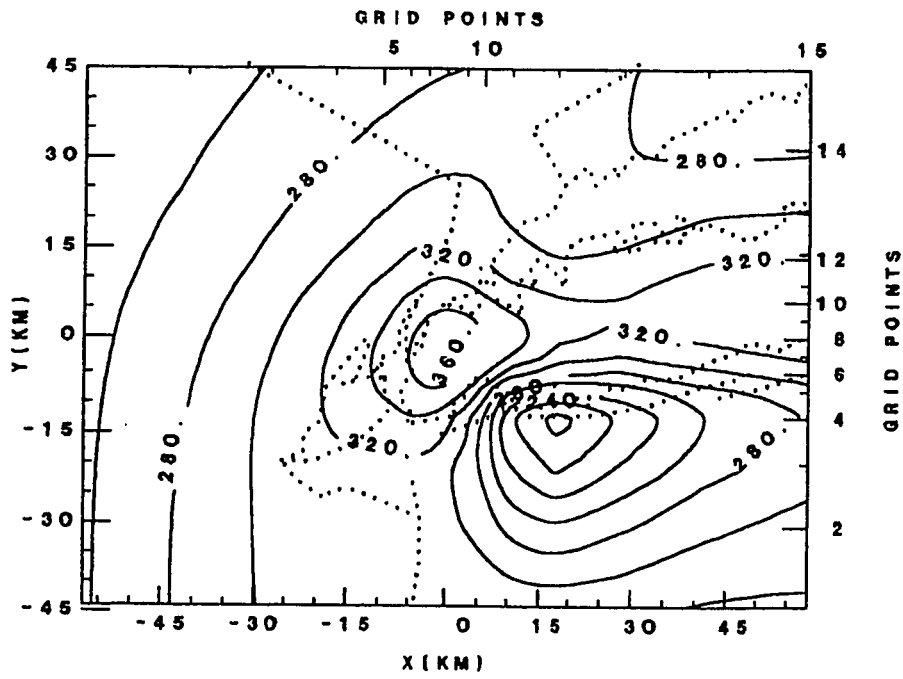


Fig. 15

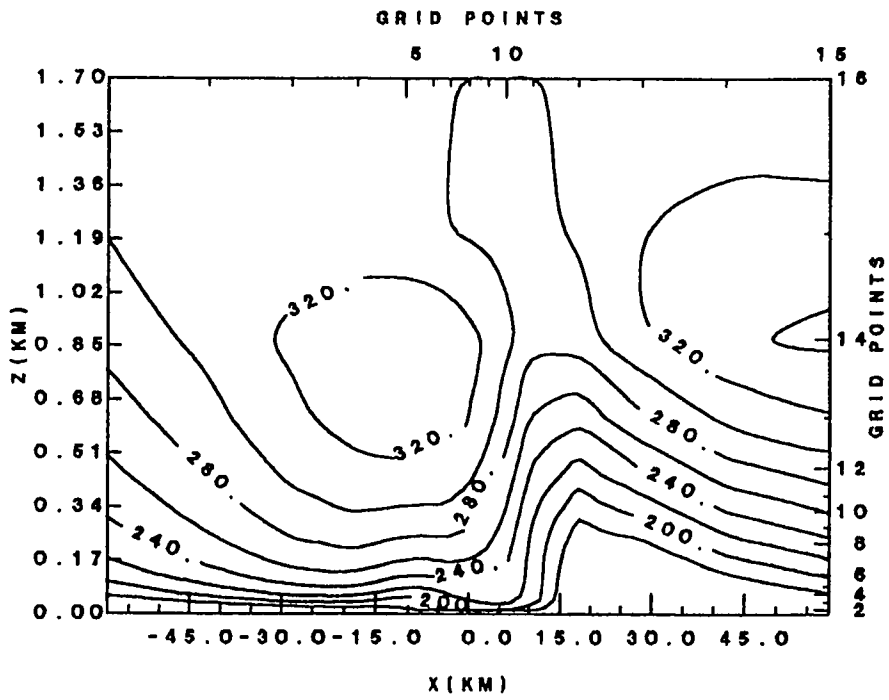


Fig. 16

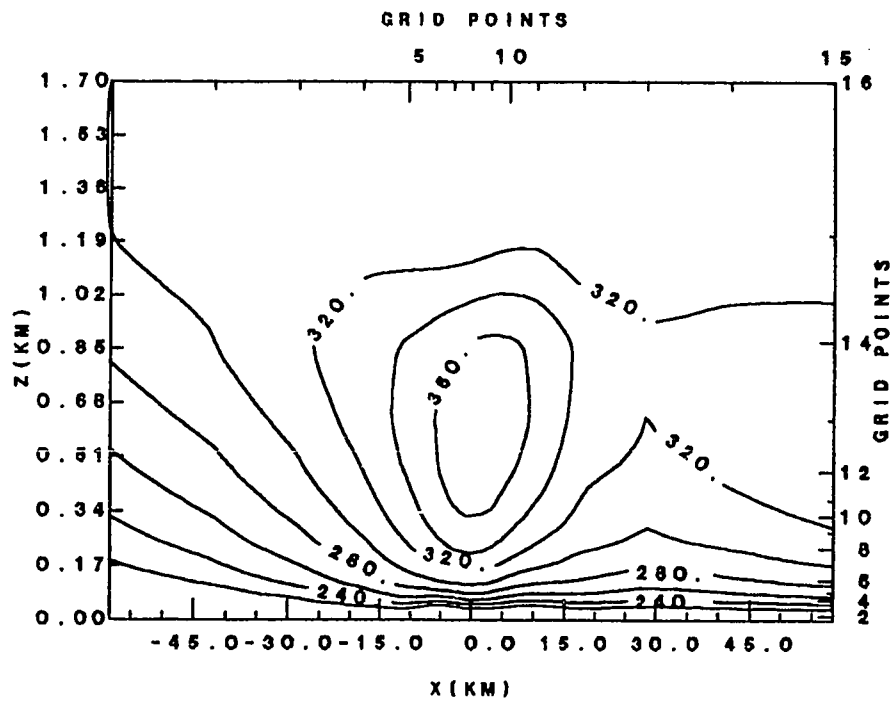


Fig. 17

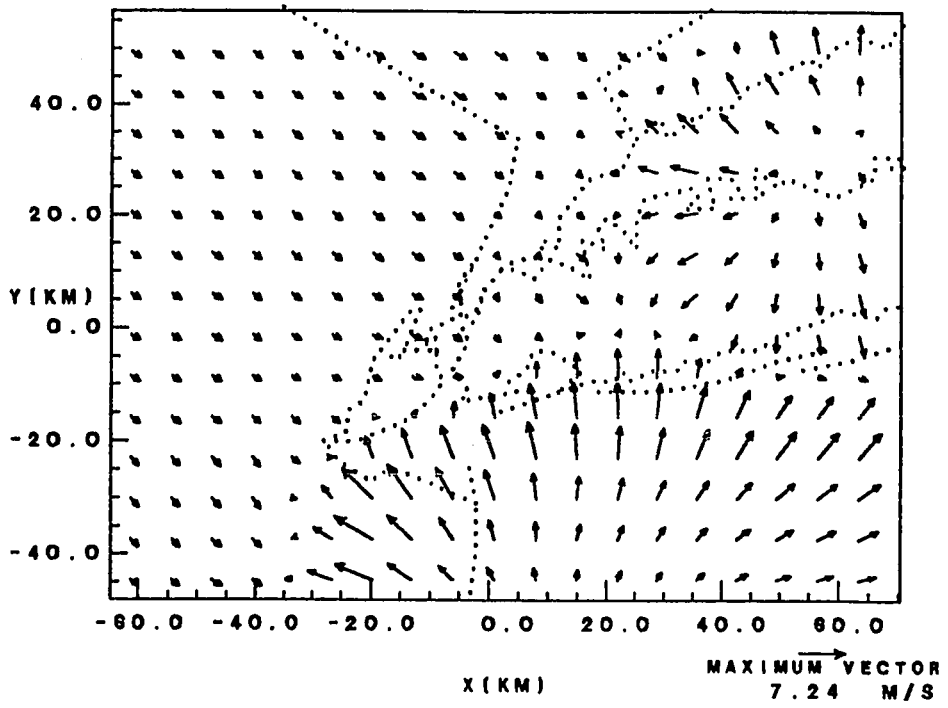


Fig. 18

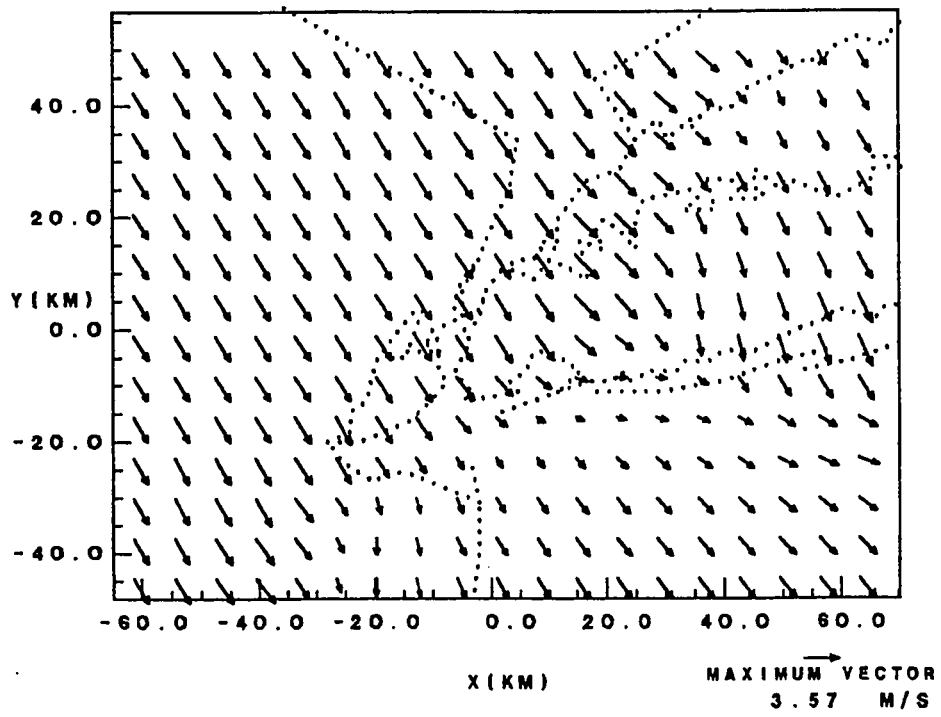


Fig. 19

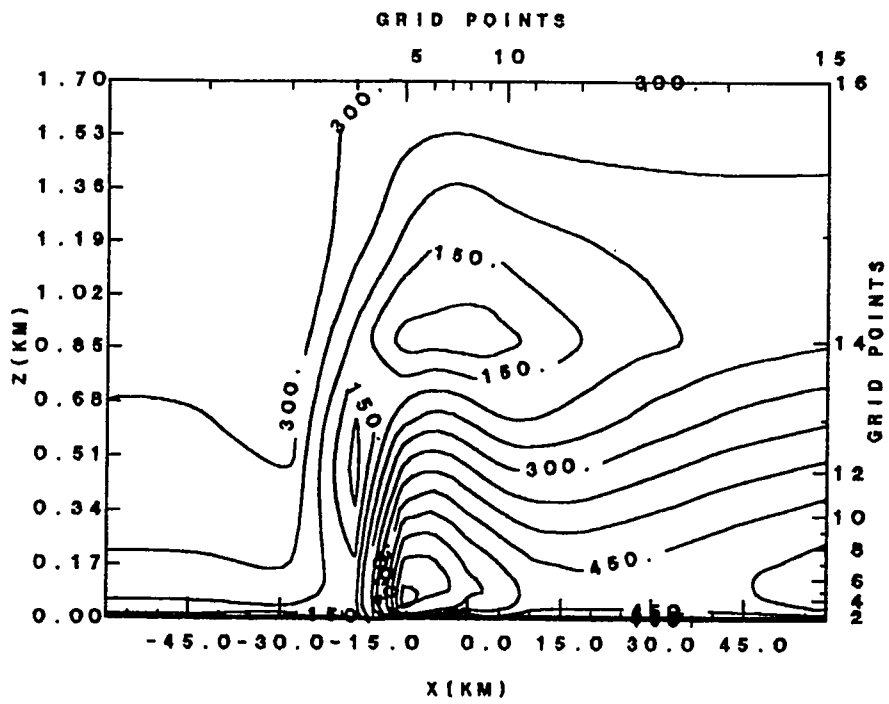


Fig. 20

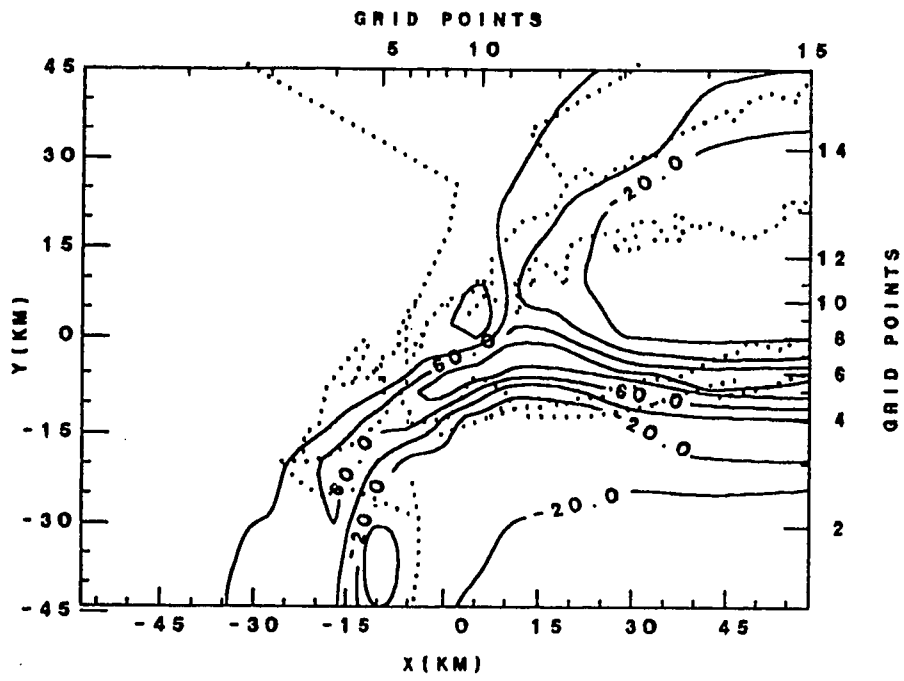


Fig. 21

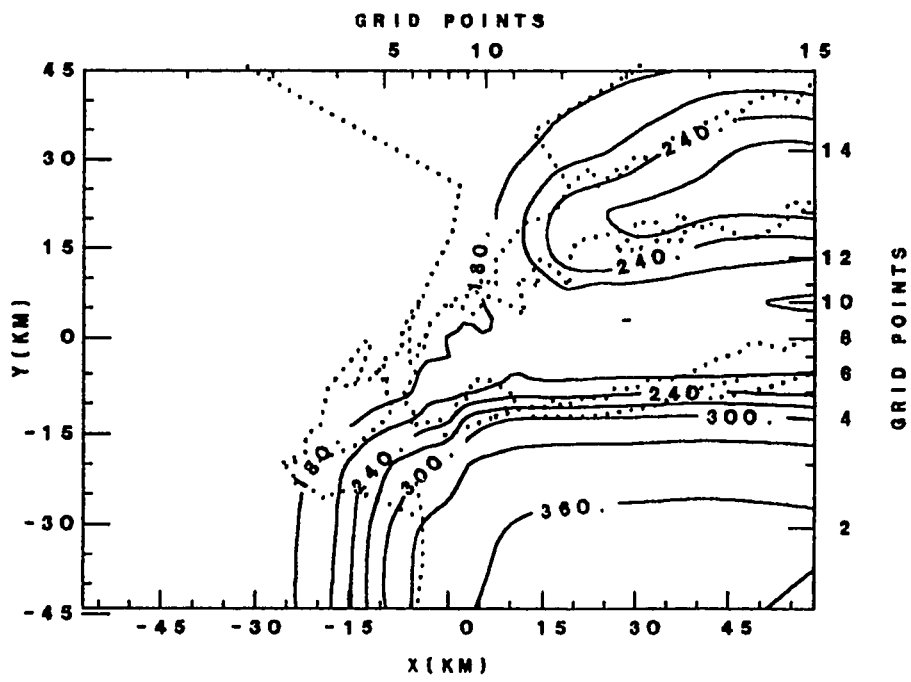


Fig. 22

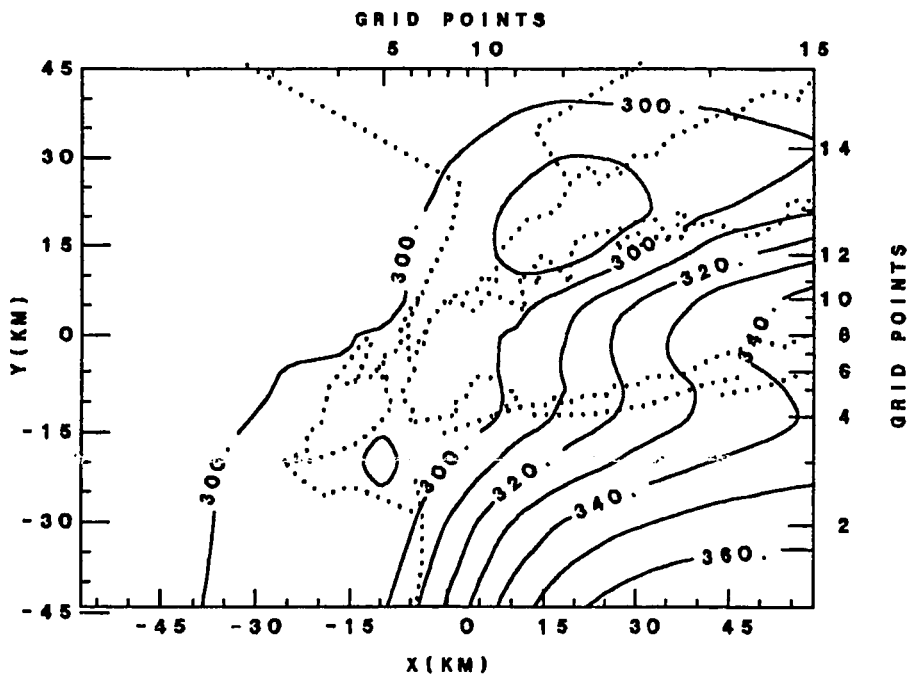


Fig. 23

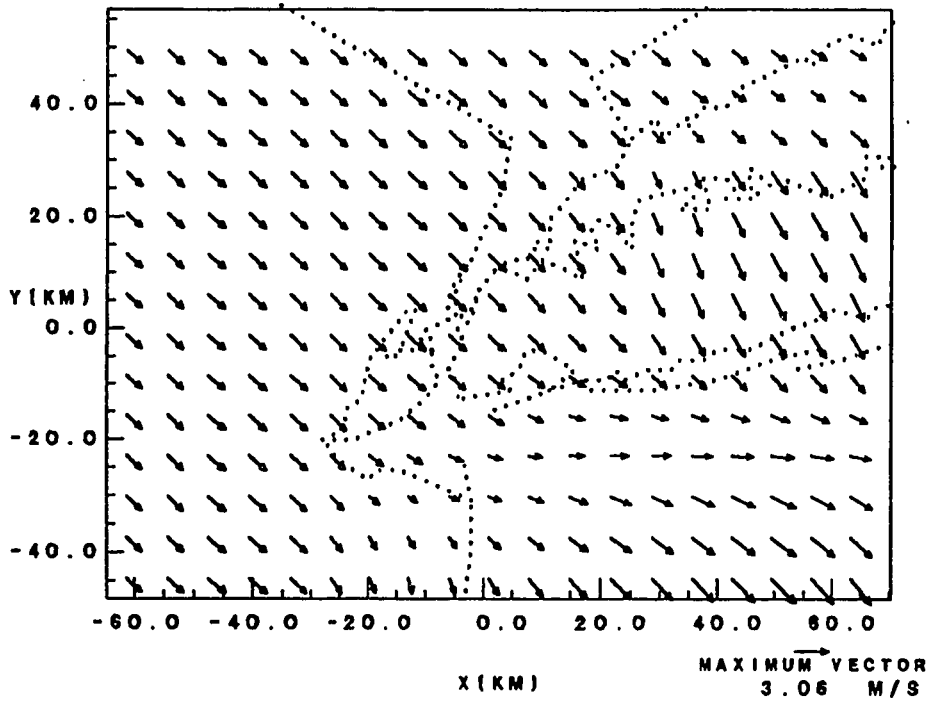


Fig. 24

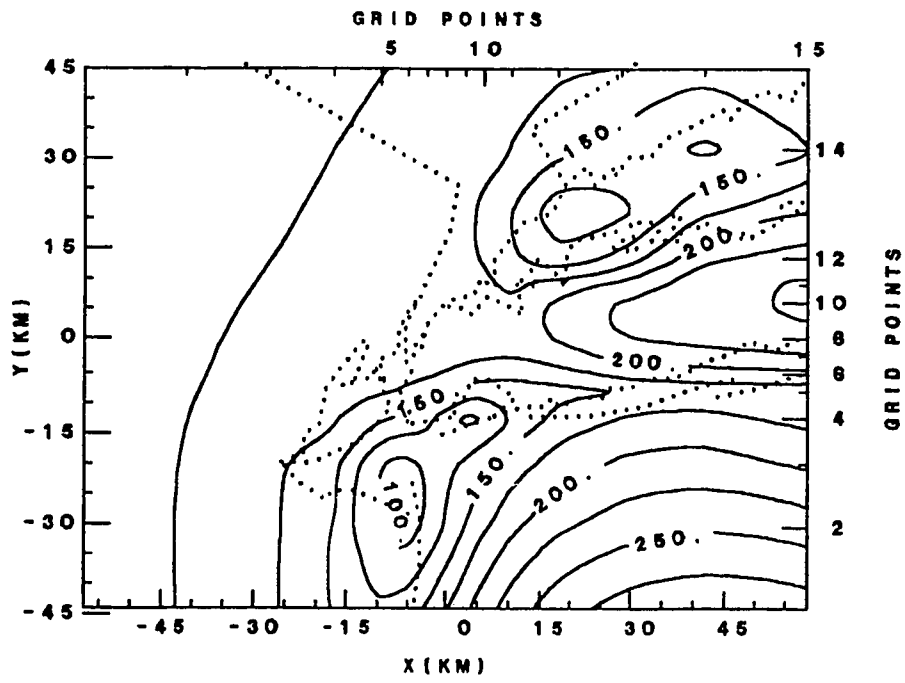


Fig. 25

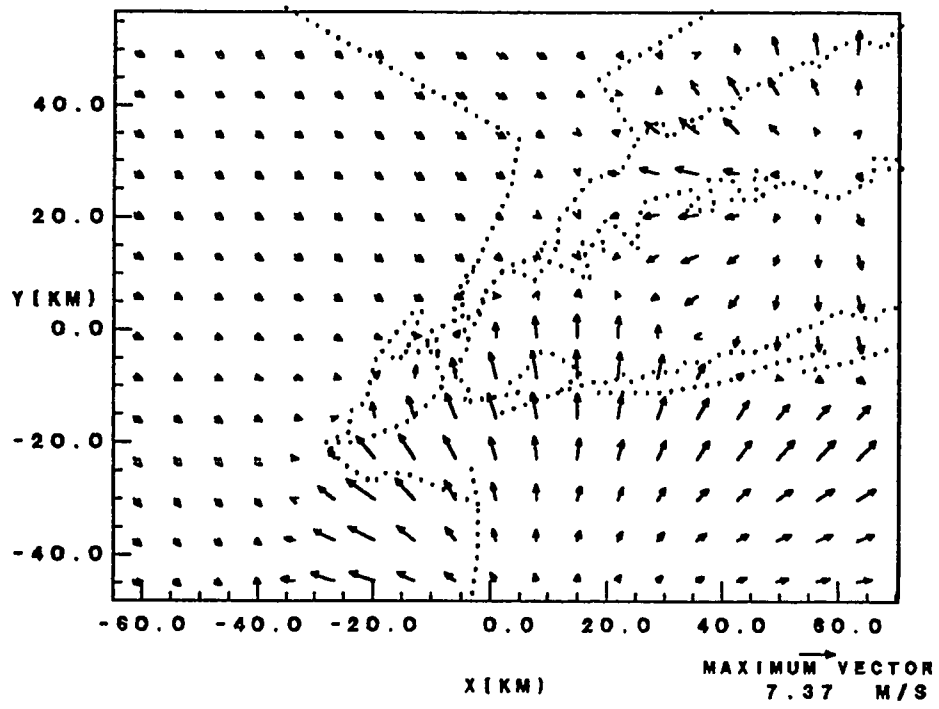


Fig. 26

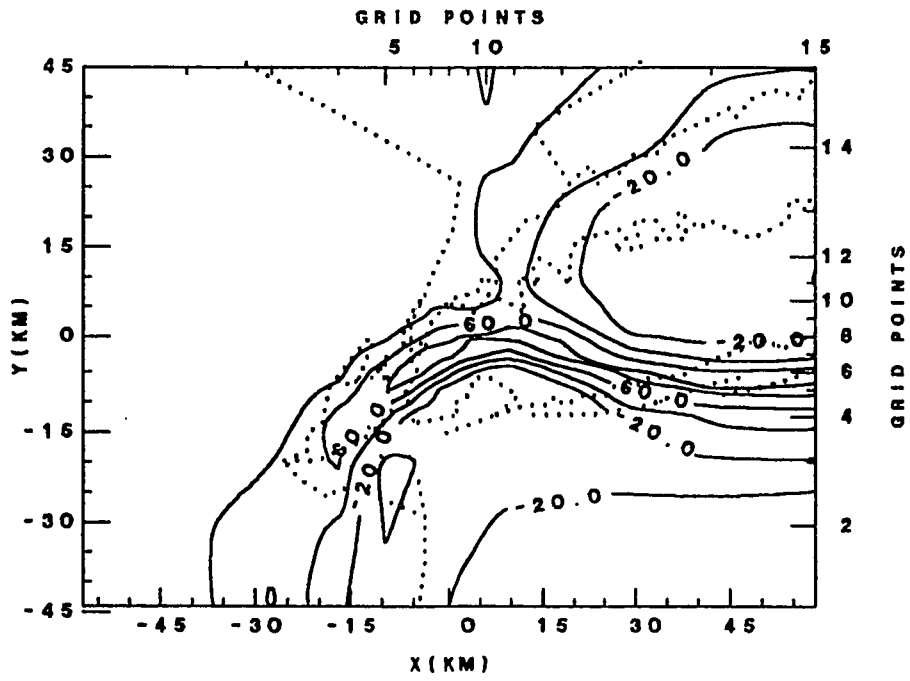


Fig. 27

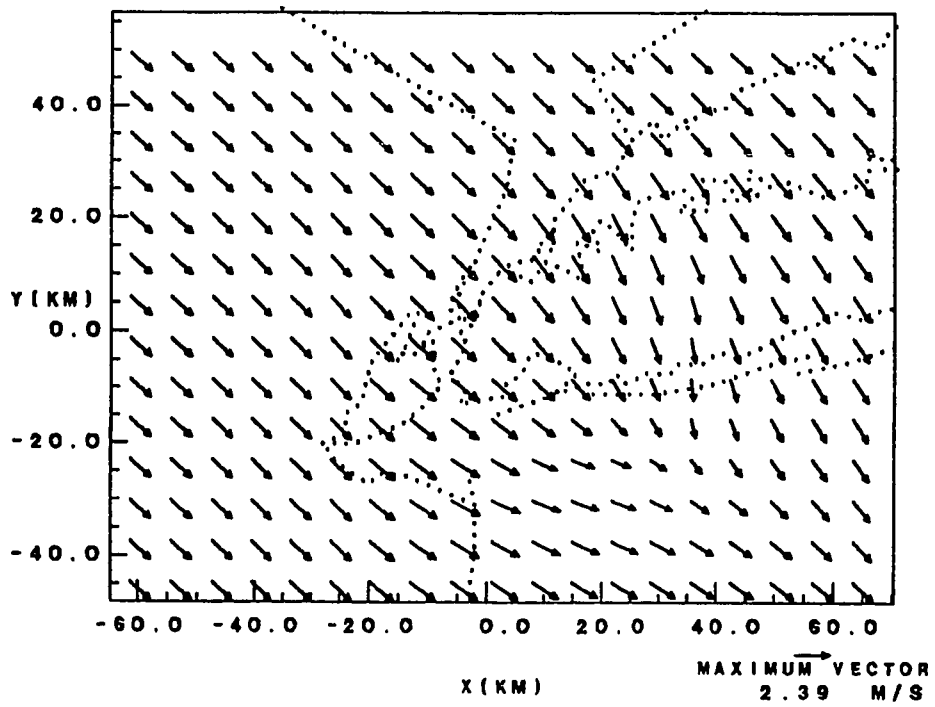


Fig. 28

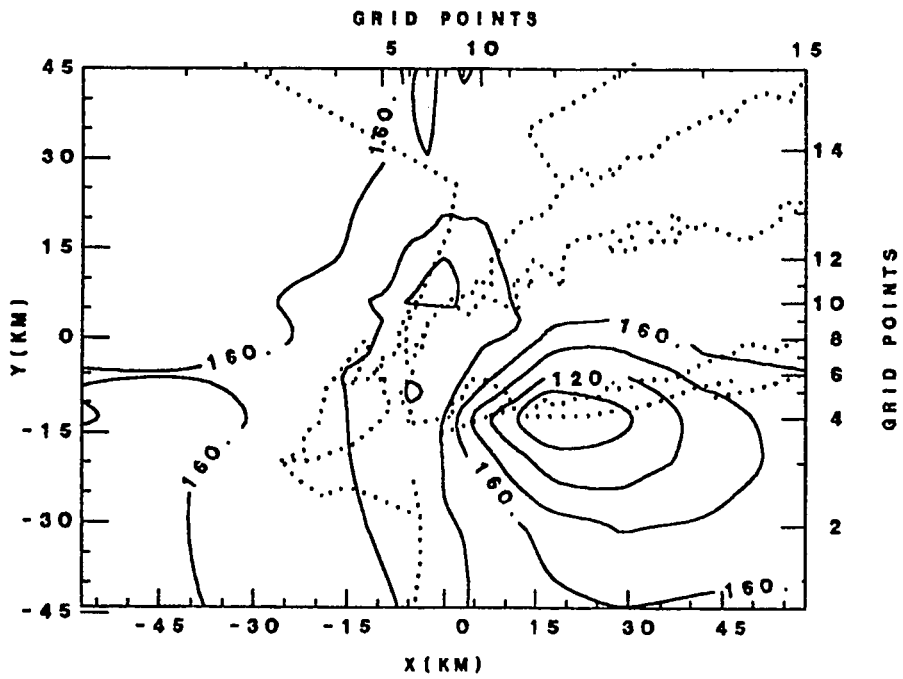


Fig. 29

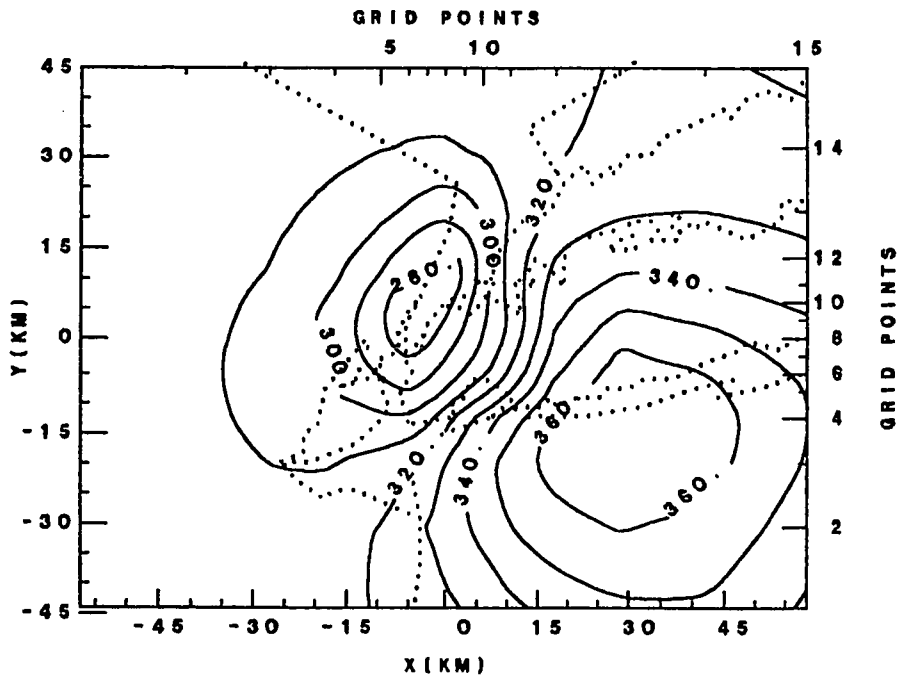


Fig. 30

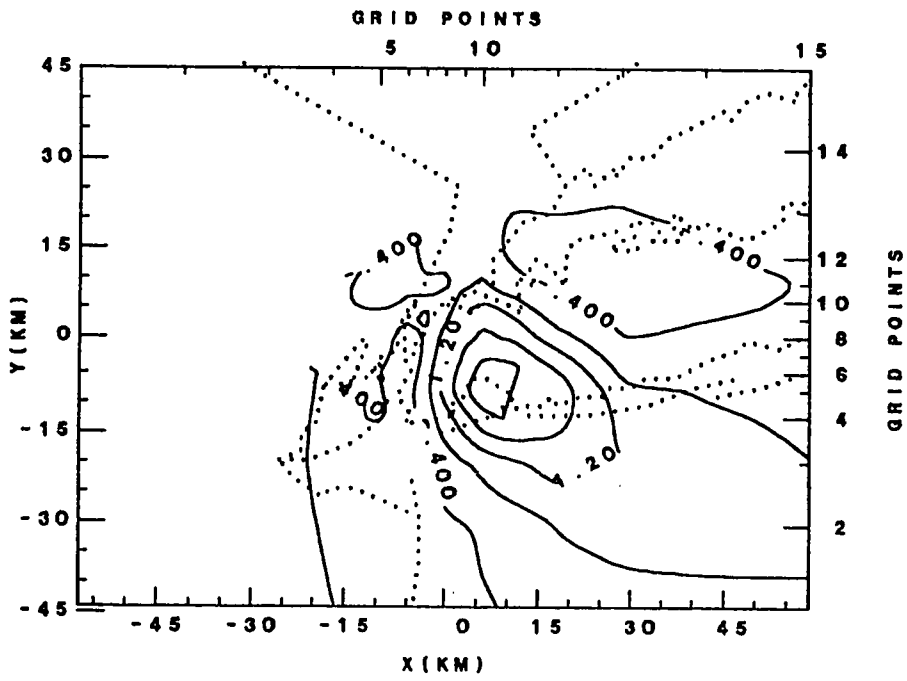


Fig. 31

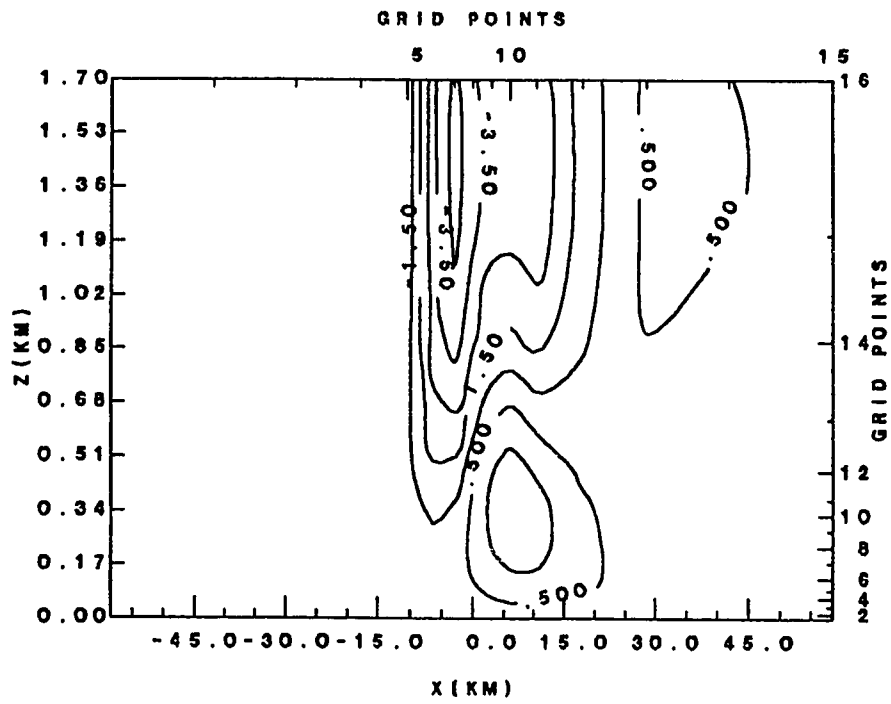


Fig. 32

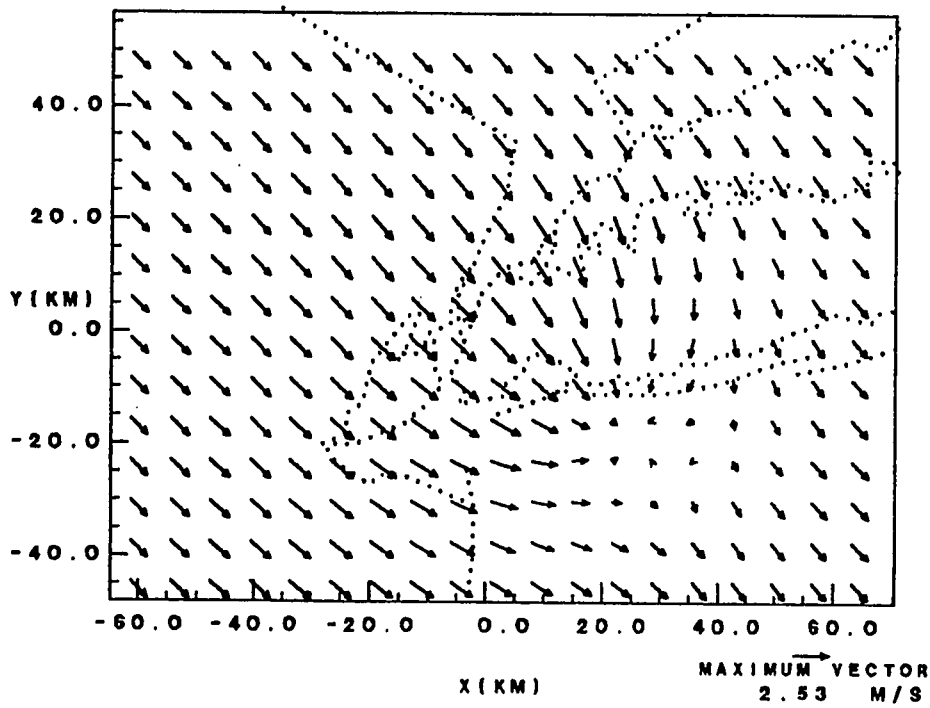


Fig. 33

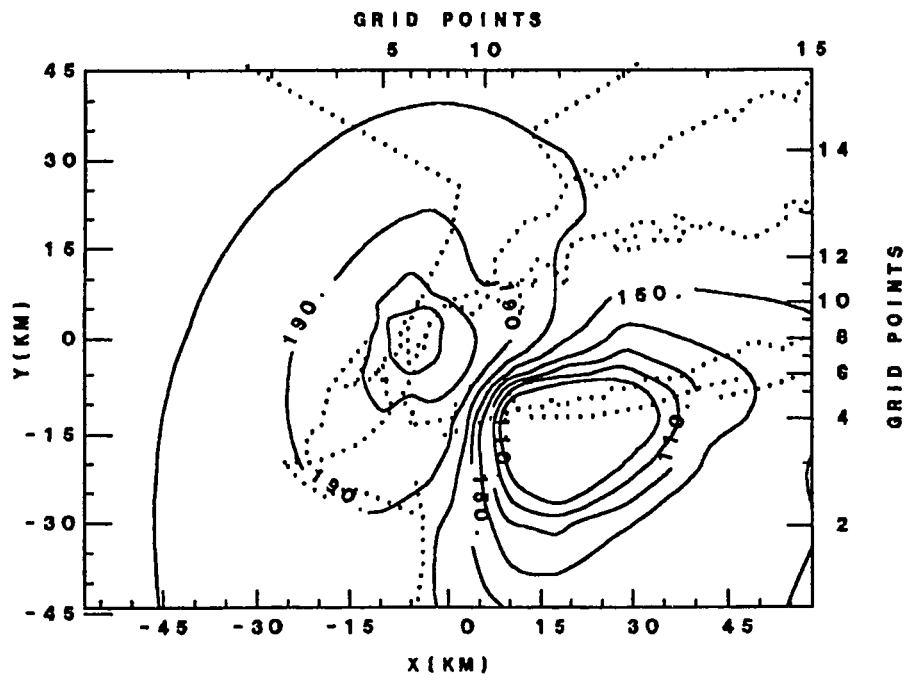


Fig. 34

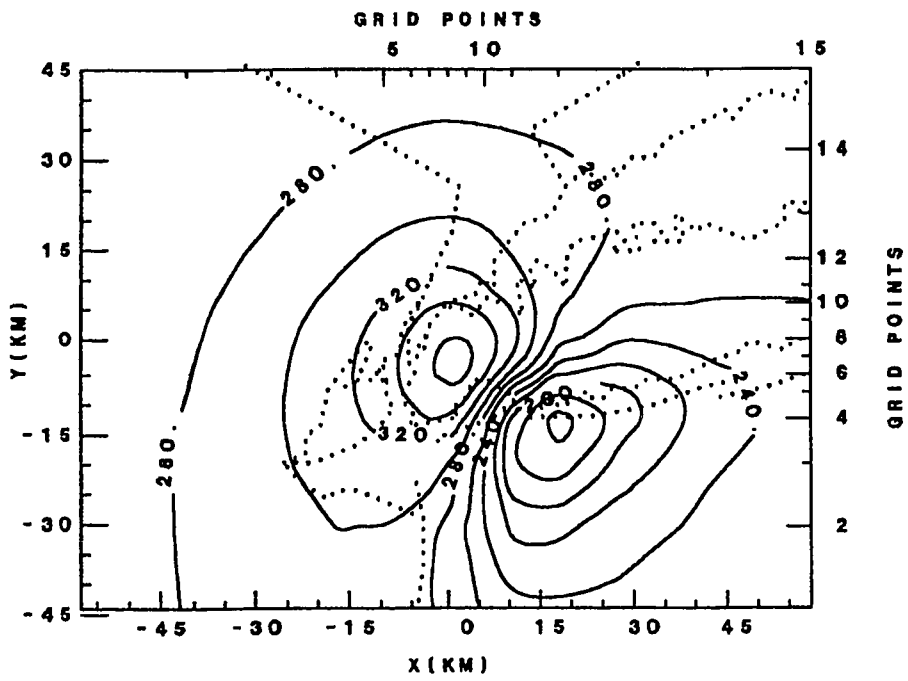


Fig. 35